

Global Patterns of Bias in Ocean Mixing Parameterization Identified Through Unsupervised Machine Learning

Ratnaksha Lele¹, Sarah G. Purkey², Jennifer A MacKinnon³, and Jonathan D Nash⁴

¹Scripps Institution of Oceanography, UC San Diego

²Scripps Institution of Oceanography, UCSD

³Scripps Institution of Oceanography

⁴Oregon State University

November 8, 2023

1 **Global Patterns of Bias in Ocean Mixing**
2 **Parameterization Identified Through Unsupervised**
3 **Machine Learning**

4 **Ratnaksha Lele ¹, Sarah G. Purkey ¹, Jennifer A. MacKinnon ¹, Jonathan D.**
5 **Nash ²**

6 ¹Scripps Institution of Oceanography, University of California San Diego, La Jolla, CA

7 ²College of Earth, Ocean and Atmospheric Sciences, Oregon State University, Corvallis, OR

8 **Key Points:**

- 9 • Unsupervised machine learning identifies clusters with distinct shear and strain
10 spectral energy transport across wavenumbers.
11 • Geographical distribution shows horizontal and vertical preferences in some of the
12 identified clusters.
13 • Two clusters diverge significantly from GM spectra identify regions of biases in
14 finescale parameterizations.

Abstract

Turbulent mixing in the ocean is often parameterized in terms of the downscale energy transfer by internal waves. Expressed in terms of the vertical wavenumber spectrum of oceanic velocity shear (V_z^2) and isopycnal strain (ζ_z^2), the "finescale parameterization" relies on several parameters, including key assumptions relating to the spectral properties. Here we use an unsupervised learning model to identify spatial correlations between embedded parameters of the finescale parameterization based upon data from 1875 full-depth hydrographic profiles from 15 sections traversing the global ocean. The clustered patterns along the sections have marked horizontal and vertical spatial dependence associated with distinct modes of spectral variation. Two clustered regions are identified where the underlying spectra deviate significantly from the canonical Garrett-Munk (GM) spectrum, suggesting potential departures from implicit assumptions about the downscale energy cascade. Spectral composites in these two regions show intensification of variance in the low and high wavenumber regimes respectively, as well as distinction in overall spectral levels and geographic prevalence. Furthermore, these clusters are found to be associated with regions where parameterized estimates of the turbulent dissipation rate ϵ differ significantly (exceeding a factor of 5) from co-located in-situ observations measured using χ -pod temperature microstructure. Extending the methodology to other hydrographic datasets has the potential to reveal reasons for this parameterization bias and to identify the dynamical underpinnings leading to more robust parameterizations of oceanic turbulent mixing.

Plain Language Summary

Turbulent mixing caused by breaking internal waves is the primary driver of the vertical heat transport and is critical for closing the ocean's energy budget. To circumvent the complexities in obtaining in-situ measurements of mixing, simplified parameterized models to estimate the rate of mixing are widely used by utilizing relatively easily collected oceanic properties such as temperature and velocity as inputs. However, inaccuracies in predictions by these simplified models arise when certain assumptions in the model are violated. In this study, by incorporating data collected from a global suite of ship based observations, we use a data-driven approach to identify the spatial distribution of two distinct regions in the ocean where large biases in the predictions by the simplified models are possible. Extending this approach, future studies could potentially identify the underlying causes of such disparities to further improve models of turbulent mixing in the ocean.

1 Introduction

Turbulent mixing plays a critical role in the overturning circulation of the global ocean, driving the vertical and horizontal transport of heat and tracers (Ganachaud & Wunsch, 2000; Wunsch & Ferrari, 2004). While mixing at the molecular level can be explicitly characterized by thermodynamic diffusion equations, the observed interior ocean stratification requires vigorous turbulent mixing that is 10-100 times stronger than that from molecular diffusion alone (e.g., W. H. Munk, 1966; Bryan, 1987; Talley, 2003; Cimoli et al., 2023), driven primarily through breaking internal waves (K. L. Polzin et al., 1997; Kunze et al., 2006; Whalen et al., 2012; Waterhouse et al., 2014; MacKinnon et al., 2017). The strength of this turbulent mixing is governed by distinct physical and dynamical processes which result in rich geographical patterns of mixing throughout the global ocean. (K. L. Polzin et al., 1997; Naveira Garabato et al., 2004; Whalen et al., 2012; Waterhouse et al., 2014; Whalen et al., 2018).

Resolving the spatiotemporal patterns of turbulent mixing in the ocean from observations is significantly challenging owing to the intermittent nature of mixing. At present,

64 the most accurate estimates of turbulent mixing come from specialized microstructure
 65 instrumentation deployed from ships (K. L. Polzin et al., 1997; St. Laurent et al., 2012;
 66 Naveira Garabato et al., 2019; Lele et al., 2021), on moorings (Moum & Nash, 2009), and
 67 autonomous platforms (Rudnick et al., 2013; Johnston & Rudnick, 2015; Shroyer et al.,
 68 2016). These microstructure instruments allow for estimates of kinetic energy dissipa-
 69 tion rate (ϵ) and temperature gradient variance (χ) by measuring high-frequency veloc-
 70 ity and/or temperature gradients. The resolved turbulent gradient spectra in the iner-
 71 tial subrange of turbulence are then used to compute ϵ and χ (e.g., Oakey, 1982; Gregg,
 72 1999; Itsweire et al., 1993). However, global microstructure observations have sparse global
 73 spatio-temporal coverage (Waterhouse et al., 2014).

74 In response to the low abundance of microstructure observations, the community
 75 has embraced a set of mixing parameterizations based upon internal wave-wave inter-
 76 action theories called finescale parameterizations that allow for the estimate of ϵ from
 77 lower resolution temperature and salinity data (Henyey et al., 1986; Gregg, 1989; K. L. Polzin
 78 et al., 1995). These parameterizations estimate turbulent dissipation of energy by esti-
 79 mating the rate of downscale energy transfer through wave-wave interactions by com-
 80 bining the measured internal wave spectral level and theoretical and empirical models
 81 of wave interactions. The applicability of finescale parameterizations on the more widely
 82 available oceanographic ship-based and Argo-based Conductivity Temperature Depth
 83 (CTD) and Lowered Acoustic Doppler Current Profiler (LADCP) data has drastically
 84 increased the spatial coverage of mixing estimates as well as our understanding of the
 85 spatial geography of mixing in the ocean (e.g., Whalen et al., 2015; Kunze, 2017b) with
 86 overall broad agreement with measurements obtained from microstructure instrumen-
 87 tation (e.g., K. L. Polzin et al., 1995, 2014; Whalen et al., 2015; Whalen, 2021) Crucially
 88 for our work, the spectral energy level is estimated by comparing the *average* spectral
 89 level within a limited wavenumber band to the idealized Garrett-Munk (GM) model (Garrett
 90 & Munk, 1972; W. Munk, 1981). Since the finescale parameterizations are referenced to
 91 the GM model in their formulation of spectral energy transport through the internal wave
 92 vertical wave number space, large departures from the GM model are susceptible to en-
 93 gendering biased estimates (K. L. Polzin et al., 2014).

94 Dissipation rates ϵ and related eddy diffusivities κ obtained from finescale param-
 95 eterizations show overall broad agreement with measurements obtained from microstruc-
 96 ture instrumentation (e.g., K. L. Polzin et al., 1995, 2014; Whalen et al., 2015; Whalen,
 97 2021), however, some discrepancies and biases have also been previously documented (e.g.,
 98 MacKinnon & Gregg, 2003; Waterman, Polzin, Naveira Garabato, et al., 2014). The un-
 99 derlying assumptions of the parameterizations are violated in many regions of the ocean,
 100 such as in the surface mixed layer, or where turbulent mixing is controlled by double dif-
 101 fusion, hydraulic jumps and strong wave-mean flow interactions over rough topography
 102 (Waterman, Polzin, Naveira Garabato, et al., 2014; K. L. Polzin et al., 2014). There are
 103 also regions where the parameterized mixing rate does not match that observations from
 104 microstructure for unclear reasons. A hypothesis considered here is that deviations of
 105 the spectral shape or other properties of the internal wave spectrum from the assumed
 106 GM form may be relevant (Müller & Liu, 2000; K. L. Polzin & Lvov, 2011), or variabil-
 107 ity in other individual parameters of the parameterization themselves, based on the lo-
 108 cal geography, topographic conditions and the presence of external forcing to the local
 109 internal wave field (Waterman, Polzin, Naveira Garabato, et al., 2014; Chinn et al., 2016;
 110 Pollmann, 2020). Recently, both supervised and unsupervised learning approaches have
 111 been used across a variety of fluid mechanical applications to provide new insight into
 112 fundamental relationships and patterns of variability in our oceans (Giglio et al., 2018;
 113 Brunton et al., 2020; Callaham et al., 2021; Kaiser et al., 2022; Mashayek et al., 2022).
 114 In particular, clustering techniques have proven useful in generating insights and explor-
 115 ing existing oceanographic data such as categorizing datasets of temperature-salinity pro-
 116 files (e.g., Rosso et al., 2020; Jones et al., 2019; Boehme & Rosso, 2021), classifying global

117 ecological marine provinces (Sonnewald et al., 2020) and identifying dominant dynamical
 118 balances in global ocean circulation models (Sonnewald et al., 2019).

119 In this study, we employ unsupervised learning to characterize a parameter-space
 120 associated with large mismatches between finescale and microstructure observations of
 121 oceanic turbulent mixing. Drawing inspiration from unsupervised learning approaches
 122 in the spectral domain applied to earthquakes and astronomical observations (Johnson
 123 et al., 2020; Ivezic et al., 2014), we use latent features extracted from oceanic shear and
 124 strain spectra as well as other variables (features) used in the formulation of finescale
 125 parameterizations to identify regions of distinct co-variations connected to properties of
 126 turbulent mixing in the ocean and underlying dynamics of internal wave-wave interac-
 127 tions. The curated hydrographic dataset used in the study is described in Section 2, with
 128 the underlying principles of finescale parameterizations, feature development, dimension-
 129 ality reduction and clustering model laid out in Section 3. Finally, we describe the ge-
 130 ography and spatial characteristics of the clustering results and the interpretation of the
 131 results in the context of the underpinning finescale parameterization for estimating tur-
 132 bulent mixing in the ocean in Sections 4 and 5.

133 2 Data

134 2.1 Ship-based Hydrographic Data

135 The principal data used in this study are 1875 profiles of high-quality full-depth
 136 CTD and LADCP data collected along 15 hydrographic sections from around the globe
 137 as part of either the Climate and Ocean Variability, Predictability and Change (CLIVAR)
 138 or the Global Ocean Ship-based Hydrographic Investigations Program (GO-SHIP) pro-
 139 grams, between the years 2000 and 2021 (Figure 1, Table 1). The horizontal station spac-
 140 ing between CTD casts is nominally 55 kilometers, with stations spaced closer in regions
 141 of interest (e.g. trenches, rough topography, boundary current regions). Vertically, the
 142 CTD-cast data used here include the profile from 500 m down to a maximum depth, usu-
 143 ally 6000 m, or to within 10-20 m from the seafloor. The top 500 m of the profiles are
 144 not considered in order to remove the surface mixed layer. Conservative temperature (θ),
 145 squared buoyancy frequency (N^2), and potential density ρ_θ are calculated from the CTD
 146 instrumentation using the Gibbs-Seawater Oceanographic Toolbox (McDougall, 2011;
 147 Jackett & McDougall, 1997). The publicly available LADCP data product has an 8-meter
 148 vertical resolution pre-processed using procedures laid out for the GO-SHIP program (Visbeck,
 149 2002; Thurnherr et al., 2010). The LADCP data product for all 15 sections contains data
 150 binned at a nominal 1-meter resolution and with horizontal (U,V) and vertical compo-
 151 nent (W) of ocean velocity from the ocean surface down to the maximum CTD depth.
 152 All LADCP data obtained are co-located with CTD data for each CTD cast along the
 153 sections.

154 2.2 Microstructure mixing estimates from CTD-mounted χ -pods

155 Estimates of ϵ from rosette-mounted microstructure χ -pods taken along the P06
 156 section were obtained from cchdo.edu (see data availability statement). ϵ was estimated
 157 using the high wavenumber temperature gradient fluctuations dT'/dz measured by the
 158 100Hz FP07 thermistor probe following the methods of Moum and Nash (2009) and Lele
 159 et al. (2021). The data have all been processed and cleaned including (1) removing any
 160 points with platform-induced noise, (2) calculating dissipation rates of the temperature
 161 variance, χ in 1-s bins, (3) any data in regions of very weak stratification where dT'/dz
 162 is less than 10^{-4} K m $^{-1}$ was removed, (4) ϵ was calculated from χ following Osborn and
 163 Cox (1972) and (5) data were binned into 200-m half overlapping segments, ensuring binned
 164 averages comparable binned finescale parameterization data (see Section 3.1).

3 Methods

3.1 Estimating Mixing from Finescale Parameterizations

Profiles of ϵ and κ are estimated from 1875 CTD stations containing a total of 64816 spectral estimates of internal wave shear $\langle V_z^2 \rangle$ and strain $\langle \zeta_z^2 \rangle$ variances using the finescale parameterization method following Gregg (1989); Henyey et al. (1986); K. L. Polzin et al. (1995); Kunze et al. (2006). Shear and strain variances are computed from CTD temperature and salinity and LADCP horizontal velocities profiles along the sections. Variance levels relative to the canonical Garrett-Munk (GM) spectra (W. Munk, 1981) are used to relate vertical turbulent eddy diffusivity (κ) to the turbulent kinetic energy dissipation rate ϵ via the Osborn (1980) relationship $\kappa = \Gamma \frac{\epsilon}{N^2}$, wherein mixing efficiency Γ considered to be nominally 0.2 (K. L. Polzin et al., 2014) and N is the buoyancy frequency. This relationship is further broken down as:

$$\kappa = \kappa_0 E_{v_z} h(R_\omega) J(f/N), \quad (1)$$

with

$$E_{v_z} = \frac{\langle V_z^2 \rangle^2}{\langle V_z^2 \rangle_{GM}^2} \quad (2)$$

$$h(R_\omega) = \frac{3(R_\omega + 1)}{2\sqrt{2}R_\omega\sqrt{R_\omega - 1}} \quad (3)$$

$$J(f/N) = \frac{f \cosh^{-1}(N/f)}{f_{30} \cosh^{-1}(N_0/f_{30})} \quad (4)$$

where \cosh^{-1} is the inverse hyperbolic cosine function, and constant values $\kappa_o = 5 \times 10^{-6} \text{m}^2 \text{s}^{-1}$, $f_{30} = 7.292 \times 10^{-5} \text{rad s}^{-1}$ and $N_0 = 5.2 \times 10^{-3} \text{rad s}^{-1}$, where f_{30} , N_0 and κ_o denote the Coriolis frequency at 30°N latitude, the canonical GM buoyancy frequency and background diffusivity respectively.

The angle brackets in Equation 2 indicate integration of LADCD-derived shear spectra over a wavenumber band capturing finescale internal wave shear variance (Gregg, 1989; K. L. Polzin et al., 2014). The factor $J(f/N)$ in Equation 1 is a latitudinal correction applied to account for weaker turbulent dissipation rates found near equatorial regions (Henyey et al., 1986; Gregg et al., 2003), while the factor $h(R_\omega)$ in Equation 3 accounts for deviations from the GM spectrum based on the frequency content of the internal wave field given by R_ω , reducing to unity when R_ω is set to the canonical GM value of 3 (K. L. Polzin et al., 1995). The dependence on strain $\langle \zeta_z^2 \rangle$ is introduced in the parameterization through the shear to strain variance ratio $R_\omega = \frac{\langle V_z^2 \rangle}{N \langle \zeta_z^2 \rangle}$, a measure of the internal wave fields aspect ratio or frequency content. This, under a monochromatic wave assumption, can be summarized as:

$$\frac{\omega}{f} = \sqrt{\frac{R_\omega + 1}{R_\omega - 1}} \quad (5)$$

representing the contribution of near-inertial ($\omega/f \approx 0$) to non near-inertial internal waves in the domain.

Profiles of ϵ and κ are calculated at each CTD station along the section from 200-m half-overlapping segments in depth using the parameterization given by Equation 1. It is important to note, however, that these parameterized estimates of diffusivity κ and dissipation rate ϵ do not sufficiently resolve mixing processes in the boundary layer, hydraulic jumps, double diffusion or internal wave driven turbulence in regimes with significant wave-mean flow interaction (Waterman, Polzin, Naveira Garabato, et al., 2014) and they produce spatially averaged estimates of mixing over multiple wave periods.

3.2 Feature Development

Here, we define and extract features from various attributes of the parameterization, to examine and understand the patterns of their cross-covariances as they relate to internal-wave driven mixing in the global ocean using unsupervised machine learning.

Building upon the parameterization in Equation 1 as the basis for feature development, we focus on measured shear and strain spectra which are the primary components of the parameterization. Buoyancy frequency normalized shear $[\phi_{V_z}]$ and strain $[\phi_{\zeta_z}]$ wavenumber spectra are calculated from the Fourier transforms of the vertical LADCP and CTD data for shear and strain respectively. To calculate shear variance $\langle V_z^2 \rangle$, segments are constructed starting from the bottom in 320 m half-overlapping windows, each tapered with a 10% sine² window function to obtain its vertical wavenumber spectra (Kunze et al., 2006), which are then integrated between wavelengths of 320 m and 150 m to avoid high wavenumber instrument noise contamination (Kunze et al., 2006).

Strain is calculated from the buoyancy frequency as $\zeta_z = (N^2 - \bar{N}^2)/\bar{N}^2$, where the mean stratification \bar{N}^2 is determined from quadratic fits to the profile segments (Kunze et al., 2006). Further, the strain variance is calculated by integrating the strain power spectrum between wavelengths of 150 m and up to 10 m while also satisfying strain variance $\langle \xi_z^2 \rangle < 0.2$ to avoid underestimating the variance through oversaturation of the spectrum (Gargett, 1990). $\langle V_z^2 \rangle$ and $\langle \xi_z^2 \rangle$ values are then normalized by the integrated GM model spectrum over the same respective bandwidths to represent the energy density in the internal wave field in the units of the GM energy density (Gregg & Kunze, 1991; W. Munk, 1981).

Each GM-normalized shear and strain spectrum is further normalized with its respective shear and strain variances across the finescale integration band to de-emphasize the known relationship between internal wave spectral level and stratification (Gregg, 1989; Kunze, 2017a). Further, we consolidate the dominant types of spectral variability by reducing the dimensionality of the data using Non-Negative Matrix Factorization (NMF) decomposition (Figure 1; described further in Section 3.2.1).

3.2.1 NMF Decomposition of Shear and Strain Spectra

While unsupervised learning could in theory identify clusters in any N-dimensional space, the quality of the resultant clustering formulation is directly proportional to the number of data points in the N-dimensional space. It is therefore prudent to introduce a low-rank approximation of the input N-dimensional space to reduce redundant co-variances in the data. Factor analysis and principal component analysis (PCA) are two of the many classical methods used to accomplish the goal of dimensionality reduction and detecting structures among the variables. Often the data to be analyzed are non-negative, and the low-rank data are further required to be comprised of non-negative values in order to avoid contradicting physical realities. Therefore, we reduce the dimensionality of the input spectral data using non-negative matrix factorization (NMF) (Lee & Seung, 1999; Berry et al., 2007) to decompose high-dimensional spectra of shear and strain into lower-dimensional latent spectral representations (Figure 1b). These low-dimensional embeddings (Figure 1c (green box), 2a-d) are further aggregated into a feature matrix along with other auxiliary features (Figure 2e-g) and are then used as feature inputs to the GMM model (Figure 1c, Section 3.2.2).

The decomposition aims to approximate the input data matrix \mathbf{X} , consisting of non-negative elements, comprised of n individual spectral data points each with m wavenumbers, into a low-rank non-negative approximation consisting of a latent feature matrix W and corresponding hidden coefficients H . This can be expressed as: $\mathbf{X}_{[n \times m]} \approx \mathbf{W}_{[n \times p]} \mathbf{H}_{[p \times m]}$ (Figure 1b). The matrix W can be regarded as spectral end-members whose linear com-

binations with the coefficient matrix H reconstruct the original data matrix X . The quality of the approximation of X is measured using the Frobenius norm $\|X - WH\|_F^2 = \sum_{ij} (X - WH)_{ij}^2$ and the optimization algorithm is carried out using the NMF implementation in the Python library *scikit-learn* (Pedregosa et al., 2011). In this study, the input data matrix \mathbf{X} for both shear and strain spectra consists of $n = 67816$ total spectra respectively obtained along the 15 GO-SHIP hydrographic section described earlier in Section 2.1.

It is conceivable that the reconstruction of the original spectra gets progressively better with the increase in the number of NMF components (p) i.e. the addition of more latent dimensions. In theory, the number of latent dimensions is inversely proportional to the reconstruction error- hence $p = m$ would result in a perfect reconstruction as the additional latent dimensions could in theory encode more of the information present in the original input matrix \mathbf{X} . However, here we choose $p = 2$ i.e. *two* latent dimensions to represent high dimensional ($m=10$) shear and strain spectra, as it results in the greatest decrease in the reconstruction error with respect to the number of latent dimensions while still preserving relevant spectral characteristics (not shown). Although increasing the number of latent dimensions beyond two results in a better reconstruction of the original spectral matrix \mathbf{X} , it can be counter-productive from an unsupervised learning standpoint as it can lead to inconsistencies in the final solutions produced by the clustering model often referred to as the “curse of dimensionality” (Bishop, 2006).

3.2.2 Final Feature Matrix (F)

Two NMF components each of the shear and strain spectra respectively are aggregated into a “feature matrix” F (Figure 1c) and used as input to an unsupervised learning model (Section 3.3). The sensitivity of the final results (Section 4) to the introduction of additional relevant features in the feature matrix- including the shear variance $\langle V_z^2 \rangle$, buoyancy frequency $[N]$ and internal wave aspect ratio R_w , all derived from the parameterization in Equation (1) is explored in Section 4.3. *Note:* The primary results discussed hereafter other than those specifically noted, describe the results of using only the 4 NMF components, two derived from the shear spectra and two derived from the strain spectra (Figure 1c green box, 2a-d).

3.3 Unsupervised Learning of Turbulent Mixing Data

An unsupervised machine learning clustering technique is used to identify groups with similar shear and strain spectra characteristics by applying a Gaussian Mixture Model (GMM) framework (e.g., Maze et al., 2017). The algorithm assumes the dataset with D features can be explained as derived from a mixture of K Gaussian distributions in D dimensions, where each feature represents a new dimension describing the data. The GMM model computes the parameters mean μ_k , covariance Σ_k and weights λ_k using the Expectation-Maximization algorithm in order to maximize the likelihood of the data X belonging to cluster k , denoted by the conditional probability distribution $p(k|x)$. The probability that data X belongs to the k^{th} component of the mixture of Gaussian distributions is given by:

$$p(k|x) = \frac{\lambda_k \mathcal{N}(x; \mu_k, \Sigma_k)}{\sum_{k=1}^K \lambda_k \mathcal{N}(x; \mu_k, \Sigma_k)} \quad (6)$$

with the multivariate normal Gaussian distribution given by:

$$p(x; \mu_k, \Sigma_k) = \frac{1}{\sqrt{2\pi^D |\Sigma|}} \exp \left[-\frac{1}{2} (x - \mu_k)^T \Sigma^{-1} (x - \mu_k) \right] \quad (7)$$

292 The conditional probability $p(k|x)$ in Equation 6 over all clusters k equals 1. The
 293 GMM algorithm assigns the cluster label k to the component for which this conditional
 294 probability is maximum i.e. $k = \operatorname{argmax}_x p(k|x)$. We further mask out data with a max-
 295 imum conditional probability less than 70% i.e. $k = \operatorname{argmax}_x [p(k|x) > 0.7]$ (Figure
 296 4a, gray) to avoid the possibility of having cluster labels with similar probability den-
 297 sities potentially near strong eddy or frontal forcings (Jones et al., 2019).

298 The choice of the number of clusters is a subjective one, and depends on the de-
 299 sired application of the clustering problem. The number of optimal clusters can vary widely
 300 based on the criteria used for convergence, tuning and choice of hyperparameters used
 301 (such as type of covariances), as well as the amount of data and choice of feature inputs
 302 given to the clustering algorithm. Dimensionality reduction for shear and strain spec-
 303 tra using NMF decomposition and clustering with the GMM model in this study were
 304 implemented using open-source python machine learning library scikit-learn (Pedregosa
 305 et al., 2011). We validate the optimal number of clusters outputted from the GMM model
 306 initialized with a “full” covariance matrix based on Akaike and Bayesian information cri-
 307 terion (AIC and BIC) scores (Schwarz G, 1978; Konishi et al., 2004). The AIC and BIC
 308 scores were computed for the entire feature matrix F created with the entirety of the data
 309 collected from 15 sections (not shown) as well random subsets of it for $K=2$ to $K=14$.
 310 The scores computed from 50 bootstraps of the random feature matrix subsets show a
 311 minimum between $K=7$ and $K=9$ clusters (Figure 7, purple shading). This conclusion
 312 is consistent when using a different metric for optimal clustering, the silhouette coeffi-
 313 cient (Rousseeuw, 1987) (not shown). Although we use $K=7$ as the optimal number of
 314 clusters, the final results described in Section 4 are quantitatively the same, regardless
 315 of the choice of the number of clusters between $K=7$ and $K=9$ (Section 4.3).

316 4 Results

317 Seven distinct clusters of data are identified using the GMM model, which we ex-
 318 plore to gain insight into the physical and geographical patterns relevant to turbulent
 319 mixing. We also consider the spatial structure of clusters and their correspondence with
 320 patterns of mismatch between finescale and microstructure-derived estimates to further
 321 contextualize the results. The feature matrix F input to the GMM model is comprised
 322 of only the two NMF-components of the normalized shear spectra and two NMF-components
 323 of the normalized strain spectra (Figure 1c, green box) for approximately 70,000 data
 324 points, each representing a 100-m vertical segment of data collected from 1875 profiles
 325 along 15 GO-SHIP sections (Figure 2a-d, 3a). The GMM is constrained to 7 clusters,
 326 hereafter discussed and referred to by the arbitrarily assigned cluster number. In terms
 327 of relative proportions of the assigned cluster labels- Cluster 5 was the most prevalent,
 328 followed by Clusters 4, 3, 7, 2, 1, and finally 6 (Figure 3d).

329 It is insightful to disentangle and isolate the original raw input data associated with
 330 each cluster to identify patterns that could potentially be linked to underlying physical
 331 mechanisms. We use the final clustering assignments to construct a composite average
 332 of the original “raw” shear and strain spectra belonging to each of the 7 clusters prior
 333 to any normalization and NMF decomposition (Section 3.2). The spectral data are “raw”
 334 in the sense that these spectra in their original form are the basis of the shear and strain
 335 variance ($\langle V_z^2 \rangle$, $\langle \zeta_z^2 \rangle$) calculations in the finescale parameterization described in Equa-
 336 tions 1 and 2. At the individual level, the spectral energy density of the raw spectra across
 337 all 15 sections span orders of magnitude and appear to have incoherent geographical dis-
 338 tributions and spatial dependence. However, considering the individual spectra combined
 339 with their corresponding clustering labels, we find that the average composite spectra
 340 (Figure 4 d, e) have distinct spectral shapes and unique slope and roll-off characteris-
 341 tics in vertical wavenumber space. These perceptible spectral characteristics, combined
 342 with the cluster spatial distributions and dependence hint at the potentially differing un-

derlying physical mechanisms responsible for the non-linear downscale energy transport and turbulent mixing in these regions.

4.1 Identification of Non-GM Spectral Conditions & Parameterized Mixing Bias

The finescale parameterization laid out in Equations 1-4 aims to represent nonlinear spectral energy transport in the vertical wavenumber domain based on arguments set forth by (Garrett & Munk, 1972, 1975, 1979), requiring careful treatment of deviations from this framework. The intent of parameterization is to encapsulate the nonlinear internal wave-wave interaction within a finite amplitude and vertical length scales not only well resolved by CTD and LADCP instrumentation (used for shear and strain calculation) and relatively free from contamination from instrumental noise or background stratification, but also from the effects of competing physical and dynamical processes such as near-boundaries mixing, wave-mean interaction, shear-driven mixing, double diffusion which could potentially short-circuit the downscale energy transfer and the basis of the parameterization. In observations (e.g., Gregg et al., 1993; K. L. Polzin et al., 1995; Brink, 1995; Eriksen, 1998), the wavenumber shear spectra at smaller wavenumbers (<0.1 cpm) are relatively white (flat) with roughly equal distribution of shear variance in this regime. The transition to turbulence occurs at length scales greater than 0.1 cpm governed by non-linear dynamics and shear instability-driven non-local energy transport (Gargett et al., 1981; Gregg et al., 1993). The finescale parameterization is employed to predict the turbulent dissipation from energy transport calculated at the intermediate scales (<0.1 cpm, Figure 4c, d grey vertical lines). Here, large deviations from GM-model prescriptions can induce biases in the estimates and are potentially emblematic of additional physical processes at play beyond wave-wave interactions (K. L. Polzin et al., 2014).

Composite averages of shear and strain spectra computed within each cluster across all 15 sections (Figure 4c,d, Supporting Information Figure S3,S4) reveal *two* clusters (Cluster 1 and 7) with spectral characteristics differing significantly from the other clusters and from GM model spectra. Averaged shear spectra in Cluster 1 shows spectral levels comparable to other clusters but are characterized with steep (“red”) slope compared to GM, with spectral roll-off at much lower wavenumbers and larger vertical scales than the other composites. At approximately the same vertical scales, shear spectra belonging to Cluster 7 show an enhancement in shear spectral power where the spectra appear “blue” and roll-off quite steeply after shear-enhanced hump. The shear-to-strain ratios (R_ω) implied by the Cluster 1 composite suggest a decrease in R_ω at higher vertical wavenumbers which could be interpreted as an increased contribution of high frequency waves at the lower wavenumbers using linear wave approximation (Equation 4). Studies have suggested that this is also possible due to the presence of quasi-permanent finestructure from rotating stratified turbulence (K. Polzin et al., 2003; K. Polzin & Ferrari, 2004).

The deviation from the assumptions about downscale spectral energy transport across wavenumbers in the parameterization is explored by comparing the ratio of the finescale parameterized estimates of turbulent dissipation rate ϵ to the concurrent co-located in-situ microstructure measurements of ϵ from CTD-mounted χ -pods (Lele et al., 2021) along the 2017 occupation of the P06 line within each cluster. The ratio of the two different estimates $\log_{10} \left(\frac{\epsilon_{\text{fine}}}{\epsilon_{\text{pod}}} \right)$ or the “mixing bias” along the P06 section where positive (negative) values indicate finescale over-prediction (under-prediction) compared to measurements from χ -pods (Figure 4a). The clustering from the GMM model combined with the mixing bias along the P06 are combined to produce estimates of average bias for each cluster (Figure 4c). The averaged mixing bias and 95% confidence intervals for clusters 2-6 fall well within a factor 5 (Figure 3c,dashed black line). Clusters 1 and 7 however, show a high and a low bias respectively, with average disagreement between finescale and

395 χ -pod estimates as large as an order of magnitude along P06. Further, the averaged spec-
 396 tral properties of the clusters also reveal marked deviations from their respective canon-
 397 ical GM shear and strain counterparts (Figure 4d,e). The inconsistencies between the
 398 rate of downscale energy transfer as prescribed by the GM model (e.g. Cluster 1) and
 399 possible shear-enhancing high-wavenumber energy sources (e.g. Cluster 7), serve as use-
 400 ful indicators of potential physical-dynamical processes unresolved in the finescale pa-
 401 rameterizations.

402 We use the clustering assignments from the GMM model along the P06 section (Fig-
 403 ure 4b), to compute the mixing bias for individual clusters, i.e. the averaged mixing bias
 404 corresponding to each cluster label along the section. We indicate the mean bias for each
 405 clusters with 95% confidence interval (Figure 4c, error bars) as well as the kernel den-
 406 sity estimate showing the overall distribution of the mixing bias for individual clusters
 407 (Figure 4c, violin plot). The averaged mixing bias and 95% confidence intervals for Clus-
 408 ters 2-6 fall well within a factor 5 (Figure 3c, (dashed black line)).

409 The formulation of the finescale parameterization in Equation 1 states that diffu-
 410 sivity κ and dissipation rate ϵ (through the Osborn relation, Section 3.1) are proportional
 411 to the total integrated shear variance from shear spectra $\langle V_z^2 \rangle$. Considering this relation-
 412 ship between $\langle V_z^2 \rangle$ and ϵ , the mixing biases between finescale parameterized observed along
 413 P06 between ϵ_{fine} and $\epsilon_{\chi\text{-pod}}$ likely occurs as a result of the overestimation (underesti-
 414 mation) of $\langle V_z^2 \rangle$ in locations where Cluster 1 (Cluster 7) occur (Figure 4f). In the case
 415 of Cluster 1, a “redder” than GM-like spectra (Figure 4e,f, pink line) results in an over-
 416 estimation of shear variance due to the assumed spectral shape being GM-like or flat (Fig-
 417 ure 4f, pink shading). The overestimated shear variance through the relationship described
 418 in Equation 1 engenders a highly inflated estimate of ϵ_{fine} by almost an order of mag-
 419 nitude (Figure 4c). A reverse mechanism occurs in the case of Cluster 7 in which an in-
 420 creasingly positive slope (“bluer”) compared to the GM-like spectra leads to an under-
 421 estimation of $\langle V_z^2 \rangle$ and consequently a depressed estimate of ϵ_{fine} .

422 Using limited-modes of spectral variation through the NMF decomposition along
 423 15 sections as inputs to the GMM model, we isolated *two* regions where underlying shear
 424 and strain spectra have characteristics to induce biases in parameterized mixing estimates.
 425 Spectral properties obtained in other process-based studies and certain localized envi-
 426 ronments have shown similarities to spectral features we identify here using a global dataset.
 427 Several different physical mechanics have been proposed in which non-white gradient spec-
 428 tra are associated with physics unresolved or problematic for finescale estimation (Kunze
 429 et al., 2002; Klymak et al., 2008; K. L. Polzin & Lvov, 2011; Brink, 1995; Eriksen, 1998).
 430 For example, well resolved spectra from a study around the Kergulean Plateau region
 431 (Waterman et al., 2013; Waterman, Polzin, Garabato, et al., 2014) associated with finescale
 432 overestimation exhibit steeper and rapid roll-offs at lower wavenumber attributed to strong
 433 wave-mean interactions in the region, similar to spectra found in Cluster 1. Similarly,
 434 generation or reflection at boundaries can inject shear at higher wavenumbers with loss
 435 of low-wavenumber energy and gain in high-wavenumber energy (Eriksen, 1985), as seen
 436 in composites from Cluster 7. Although diagnosing and interpreting the plethora of pos-
 437 sibilities in the physics driving such peculiarities in the spectral energy transports in wavenum-
 438 ber space is beyond the scope of the paper- we further aim to prognosticate the spatial
 439 structure distribution of regions of potential finescale mixing bias along these sections.

440 4.2 Geographical Distribution

441 The spatial distribution of the clusters shows a rich and varied geographical dis-
 442 tribution along the 15 sections considered here (Figure 3a). From a high-level perspec-
 443 tive, the clustering reveals a rough dependence on stratification as seen by the alignment
 444 in most sections with the contours of buoyancy frequency along those sections (Figure
 445 3a, black lines). Even though the inputs to the GMM consist of buoyancy-normalized

446 spectral data that have been standardized by their respective integrated variances in or-
 447 der to diminish the a priori stratification dependence, the clustering patterns neverthe-
 448 less reveal an ostensible relationship with buoyancy frequency (N).

449 In addition to the geographical cluster assignments by individual sections, more
 450 insight into the distinguishing characteristics of the clustering patterns can be gained
 451 by looking at the spatial variations in probability densities of each clusters vertically (depth
 452 and height-above-bottom) and horizontally (along-section) for each section individually,
 453 as well as by computing composites encompassing all 15 sections (Figure 3 [b-c,e-f] 5,
 454 6, Supporting Information Figure S1-S2).

455 The upper ocean was dominated by clusters 2, 3 and 4, each showing similar ver-
 456 tical distributions, with some differences in their zonal and meridional distributions. Clus-
 457 ter 2 forms the majority of clusters within the Southern Ocean, as seen by the increase
 458 in prevalence southward of 55°S along S4P, I06 and P16S, and the peak of the latitu-
 459 dinal distribution from the zonal composite found around 62.5°S (Figure 3e). No dis-
 460 tinct patterns emerge in the zonal and meridional distribution of cluster 3 and 4, sug-
 461 gesting minimal geographical precedence (Figure 3e, f). In depth, all three clusters be-
 462 come more prevalent closer to the seafloor (Figure 3c), resulting in peaks around 3000
 463 m, also reflecting the variations in bathymetry of the sections (Figure 3b). The presence
 464 of Cluster 2 in the Southern Ocean and other sections near the bottom bathymetry, for
 465 example, along the P06, P02 and A20 (Supporting Information Figure S2) is consistent
 466 with regions of low stratification and is seen clearly in the contours of buoyancy frequency
 467 along those sections (Figure 3a, black lines)

468 Above the ocean bottom, the analysis found an increase in the relative abundance
 469 of clusters 5 and 6. These two cluster are prominently found in upper ocean along most
 470 sections between 500 m and 2000 m. Cluster 6 is the least prominent of the assigned la-
 471 bels and forms only 7.8% of the total assigned clusters and is mostly found in the up-
 472 per ocean, typically between 1500 m and 2000 m in the Atlantic ocean (e.g. a13, a16n
 473 16s and a10 lines). Cluster 5 is the second most common upper ocean cluster other than
 474 Cluster 1, with no notable zonal preference.

475 Cluster 1, associated with “redder” shear spectra, is predominately found in the
 476 upper ocean along most sections, existing primarily between 500-1500 m depth (Figure
 477 3 b), with the notable exception in the Ross Sea (S4P) and Gulf of Mexico (A20) which
 478 show a second mid-depth around roughly 4000 m (Figure 3a, Supporting Information
 479 Figure S1). In addition, the zonal section composite also reveals a strongly increased pro-
 480 portion of Cluster 1 along the equator, with a clear peak observed within 5 degrees of
 481 the equator. In addition, the cluster is found most often in the subtropics with it rarely
 482 observed at high latitudes (Figure 3e). Meridional variability in Cluster 1 is observed
 483 with a vast preponderance in the Southern Hemisphere’s subtropical Atlantic and East-
 484 ern Pacific (Figure 3f).

485 Cluster 7, associated with “bluer” shear spectra with enhanced energy at wavenum-
 486 bers between 150-100 m, is distributed in the mid to deep oceans, forms roughly 10.4%
 487 of the total cluster labels along the 15 sections (Figure 3d) and is most prevalent above
 488 the bottom bathymetry with a peak around 500 m from the bottom bathymetry (Fig-
 489 ure 3c). Zonally, an increased proportion of cluster 7 is found in the Southern Ocean,
 490 scattered vertically throughout the sections, with cluster 7s found from the surface all
 491 the way down to the bottom topography (e.g. S4P).

492 **4.3 Sensitivity of GMM to Number of Clusters [K] and additional fea-** 493 **ture inputs[d]**

494 To test the robustness of the findings discussed above, we explore the sensitivity
 495 of this study to two key analysis choices. First, the effect of constraining the number to

496 cluster to 7 is tested, and second, the effect of adding additional features to the GMM
497 model is explored.

498 The analysis was run with a range of fixed number of clusters (K) ranging from 2
499 to 14. The optimal number of class labels requires model hyperparameter tuning, and
500 the results are shown by the BIC scores (Figure 7). The BIC score shows a minima at
501 $K=7$, but with some ambiguity for $K=7-9$. Here, we discuss sensitivity of our final re-
502 sults and conclusions to the clustering produced by the GMM model with the same four
503 spectral inputs inputs, but with $K=8$ (Labels 0-7) as the optimal number of clusters here.
504 The clustering distribution using $K=8$ and four inputs is overall very similar to the dis-
505 tribution with $K=7$. The additional 8th class label is assigned to regions in the upper
506 ocean and seems to split regions assigned to Cluster 1 in Figure 3a into two regions with
507 labels 4 and 6 (Supporting Information Figure S5a).

508 This is further supported by the mean strain and shear spectra calculated from com-
509 posite averages of individual cluster labels across the whole dataset (Supporting Infor-
510 mation Figure S5b,c). Clusters 4 and 6 are associated with shear spectra with negative
511 slopes whereas Cluster 5 (similar to Cluster 7 in Figure 3a) has a positive slope. Fur-
512 ther, we see a similar association of finescale biased ϵ with regions in Clusters 4 and 6
513 over-predicting ϵ , while regions within Cluster 5 under-predict ϵ compared to measure-
514 ments from χ -pods along the P06 section. Similarly, we tested $K=9$ (not shown) and it
515 did not change the key findings of this study. Thus, while minor qualitative differences
516 are to be expected with clustering assignments for each of the clusters with the results
517 discussed in Figure 3 and 4, we do not find any quantitative differences in the iteration
518 of results discussed above with the final conclusions of the study.

519 Second, the sensitivity of the final results to the incorporation of additional fea-
520 tures as inputs to the GMM model is explored. The decision boundaries delineating one
521 cluster from the next in the GMM model is a function of the means and covariances that
522 describe the multi-dimensional Gaussian distributions. In general, addition or subtrac-
523 tion of feature inputs to the clustering model, aside from varying the dimensionality of
524 the clustering space, can greatly affect these means and covariances and as a consequence
525 the delineation and distribution of individual clusters in space. In an effort to critique
526 the final results as not merely serendipitous artifacts attributable to the choice of fea-
527 ture inputs, various permutations of feature inputs to the GMM are explored, all derived
528 from parameters in the finescale parameterizations (Section 3.1, Equations 1-5). We com-
529 pare our main results to a GMM run using seven feature inputs consisting of four shear
530 and strain spectra NMF decompositions, shear variance $\langle V_z^2 \rangle$, buoyancy frequency (N)
531 and the internal wave aspect-ratio R_ω (Figure 2a-g) with seven output clusters (Labels
532 0-6).

533 Compared to the four feature run presented in the main text, the seven feature run
534 produces clusters that are highly correlated to buoyancy frequency as seen in the align-
535 ment with buoyancy frequency contours along most of the 15 sections (Supporting Infor-
536 mation Figure S6a, black solid lines). The results also show an overall higher poste-
537 rior probability of clustering assignment as seen in the reduction in probability mask ap-
538 plied for posterior probabilities less than 70% (Supporting Information Figure S6a, grey
539 mask). However, computing averaged strain and shear spectra composites for each clus-
540 ter as before shows two clusters associated with large deviations from the GM-model shape
541 (Supporting Information Figure S6b,c, Clusters 2 and Cluster 4). Biases in finescale ϵ
542 estimates also exist for the same two clusters with regions along Cluster 4 overpredic-
543 ting and regions along Cluster 2 underpredicting ϵ compared to observations to χ -pods
544 along the P06 section (Supporting Information Figure S6d). With no significant quan-
545 titative differences in the results relating to the finescale bias, we recentered the focus
546 of the main text on describing and discussing the results from the four-feature GMM out-
547 put (Figure 2a-d).

548 5 Conclusions

549 In this study, we use a novel unsupervised learning approach with a Gaussian Mix-
 550 ture Model (Jeff A. Bilmes, 1998; Bishop, 2006) to cluster and identify patterns of tur-
 551 bulent mixing-related features derived from fundamental constituents of finescale param-
 552 eterizations of internal wave-driven turbulent mixing in the ocean using a global dataset
 553 of ship-based hydrographic CTD and LADCP data collected on 15 GO-SHIP lines. Us-
 554 ing an NMF decomposition of oceanic shear and strain spectra, we extracted spectral
 555 features consisting of encoded information about spectral level, shapes and slopes (Sec-
 556 tion 3.2, Figure 1, 2). These features once aggregated into a feature matrix are clustered
 557 using the GMM model into seven different domains characterizing and delineating their
 558 collective variation in the N-dimensional space represented by the extracted features. The
 559 class labels roughly align with stratification in the ocean on average vary with depth and
 560 height-above-bottom across the global ocean. Latitudinal and longitudinal variations among
 561 the clusters are more convoluted.

562 Further, we explore the implications and potential effects of spectral deviations in
 563 wavenumber space from the canonical Garrett and Munk (GM) internal wave spectrum
 564 (Garrett & Munk, 1972, 1975, 1979), for application of the finescale parameterizations
 565 to global data collected along 15 GO-SHIP sections. We identify the average compos-
 566 ite shear and strain spectra associated with each of the seven clusters revealing two clus-
 567 ters (Cluster 1 and Cluster 7) associated with distinct spectra differing significantly from
 568 both the other composites and GM model in their wavenumber distribution of shear and
 569 strain spectral energy. Since the wavenumber distribution dictates the rate of energy trans-
 570 port and downscale energy transfer from large to smaller scales and ultimately to wave-
 571 breaking scales, the spectral characteristics within each cluster are ultimately tied to un-
 572 derlying physical mechanisms at play for turbulent mixing to occur in those regions. While
 573 uncovering the underlying mechanisms at play driving each cluster’s spectral distribu-
 574 tion is beyond the scope of this paper, we explore the robustness of mixing estimates ob-
 575 tained from finescale parameterizations in these regions further.

576 Studies have previously found large biases in finescale parameterized estimates where
 577 physical and dynamical environments short-circuit the underlying assumptions of the pa-
 578 rameterizations, for e.g. regions in the surface mixed layer, near boundaries or where tur-
 579 bulent mixing is controlled by double diffusion, hydraulic jumps and strong wave-mean
 580 flow interactions over rough topography (Waterman, Polzin, Naveira Garabato, et al.,
 581 2014; K. L. Polzin et al., 2014; MacKinnon & Gregg, 2003). Our analysis is consistent
 582 with prior studies regarding the broad agreement between finescale parameterized and
 583 microstructure estimates of mixing in the open ocean thermocline where the underly-
 584 ing assumptions made in the parameterizations apply (K. L. Polzin et al., 1995, 2014;
 585 Whalen et al., 2015; Waterman, Polzin, Naveira Garabato, et al., 2014). However, based
 586 on the wavenumber distribution of global oceanic shear and strain spectra, we provide
 587 a rationale behind large biases in finescale parameterized estimates as well as identify
 588 their potential global spatial distribution based on data along 15 GO-SHIP lines.

589 Two clusters associated with high and low-biased finescale ϵ estimates when com-
 590 pared to co-located temperature microstructure observations from χ -pods along the P06
 591 section were identified. The clusters are distinct in their spatial distribution along the
 592 P06 section. Cluster 1 associated with regions of finescale overestimation is primarily
 593 found in the upper ocean between 500 m and 2000 m in depth, while Cluster 7 is linked
 594 to regions of finescale underestimation and is found mostly in the deeper ocean below
 595 3000 m with an increased abundance roughly 500 m-1000 m above the bottom bathymetry
 596 (Figure 3b,c). Both along the P06 section and averaged globally, the two cluster regions
 597 consist of roughly 20% of the total clustered data.

598 More work is needed to further our understanding of the underlying dynamical pro-
 599 cesses and the geographical distribution of various flavors of internal wave-wave inter-

600 actions found in the ocean. Regardless of the cause, this study has shown that caution
 601 must be used when applying finescale parameterizations ubiquitously throughout the ocean.
 602 We show there are regions of the ocean where the prevalence of more "red" or more "blue"
 603 spectra energy could lead to biases in estimates of mixing derived from finescale param-
 604 eterization that assume a GM-like universal form. This study could serve as a template
 605 to apply unsupervised machine learning approaches to localized process-based hydrographic
 606 studies or in engineering innovative features derived from hydrographic observations in
 607 an effort to understand the geographical and spatial distribution of the underlying dy-
 608 namics.

Line	Profiles	Cluster 1	Cluster 2	Cluster 3	Cluster 4	Cluster 5	Cluster 6	Cluster 7
a20	74	2.9	9.4	17.3	28.8	22.8	6.2	12.6
a22	90	1.9	15.2	15.7	28.5	17.1	6.9	14.8
a13	128	10.2	1.5	13.1	19.3	36.5	12.9	6.4
a16n	119	8.5	1.6	12.9	18.5	35.5	15.3	7.8
a16s	111	9.5	2.2	15.0	24.7	27.4	10.6	10.6
i06	56	13.2	22.7	11.4	7.6	33.0	2.5	9.5
i08	114	5.7	12.8	13.7	16.0	34.6	5.2	12.0
i07	110	8.6	2.4	15.4	23.5	31.4	9.0	9.7
p18	209	2.6	2.9	17.5	34.9	19.2	10.5	12.4
p16s	86	8.6	20.5	11.6	14.0	29.8	2.8	12.6
p02	159	9.8	17.6	11.7	14.0	31.1	4.9	10.9
a10	116	16.5	1.6	11.6	17.0	35.7	10.9	6.7
s4p	72	0.5	36.1	11.9	19.6	9.1	3.6	19.2
p06	244	7.9	10.8	12.9	18.5	31.8	7.1	11.0
i05	187	25.3	10.8	9.7	8.2	35.7	3.0	6.3
TOTAL	1875	9.4	9.8	13.4	19.6	29.6	7.8	10.4

Table 1. Total number of full-depth profiles for each of the 15 GO-SHIP lines in the study along with the percentage distribution of each cluster from the GMM model output along a given line corresponding to results described in the main text and Figure 3.

609 Acknowledgments

610 We thank the WOCE, CLIVAR, and GO-SHIP programs for collection of the hydrographic
 611 and LADCP data used in this study. CLIVAR and GO-SHIP data were collected and
 612 made publicly available by the International Global Ship-based Hydrographic Investi-
 613 gations Program and the national programs that contribute to it. Lele was supported
 614 by the NASA FINESST program (Grant 80NSSC20K1609). Lele, Purkey, MacKinnon
 615 and Nash were supported by NSF (OCE-2023289). Purkey was also supported by NSF
 616 (OCE-2023545).

617 Open Research

618 All data used for this article are publicly available. Hydrographic and LADCP data
 619 for hydrographic lines used in this study (Table 1) can be searched by the line "num-
 620 ber" through the CCHDO (<http://cchdo.ucsd.edu>) and

621 University of Hawaii (<https://currents.soest.hawaii.edu/go-ship/ladcp/>) website.
 622 The χ -pod data collected on P06 2017 Leg 1 and 2 are available
 623 from CCHDO (<https://microstructure.ucsd.edu/#/cruise/320620170703>) and
 624 (<https://microstructure.ucsd.edu/#/cruise/320620170820>) respectively.

625 References

- 626 Berry, M. W., Browne, M., Langville, A. N., Pauca, V. P., & Plemmons, R. J.
 627 (2007). Algorithms and applications for approximate nonnegative matrix
 628 factorization. *Computational Statistics and Data Analysis*, *52*(1), 155–173.
 629 doi: 10.1016/j.csda.2006.11.006
- 630 Bishop, C. M. (2006). *Pattern recognition and machine learning*. New York :
 631 Springer, [2006] ©2006.
- 632 Boehme, L., & Rosso, I. (2021). Classifying Oceanographic Structures in the
 633 Amundsen Sea, Antarctica. *Geophysical Research Letters*, *48*(5). doi:
 634 10.1029/2020GL089412
- 635 Brink, K. H. (1995). Tidal and lower frequency currents above Fieberling Guyot.
 636 *Journal of Geophysical Research*, *100*. doi: 10.1029/95jc00998
- 637 Brunton, S. L., Noack, B. R., & Koumoutsakos, P. (2020). *Machine Learning for*
 638 *Fluid Mechanics*. doi: 10.1146/annurev-fluid-010719-060214
- 639 Bryan, F. (1987). Parameter sensitivity of primitive equation ocean general circu-
 640 lation models. *Journal of Physical Oceanography*, *17*, 970–985. doi: 10.1175/
 641 1520-0485(1987)017(0970:psopeo)2.0.co;2
- 642 Callahan, J. L., Koch, J. V., Brunton, B. W., Kutz, J. N., & Brunton, S. L. (2021).
 643 Learning dominant physical processes with data-driven balance models. *Nature*
 644 *Communications*, *12*(1016). doi: 10.1038/s41467-021-21331-z
- 645 Chatfield, C., Bendat, J. S., & Piersol, A. G. (1987). Random Data: Analysis and
 646 Measurement Procedures. *Journal of the Royal Statistical Society. Series A*
 647 *(General)*. doi: 10.2307/2981634
- 648 Chinn, B. S., Girton, J. B., & Alford, M. H. (2016). The impact of observed vari-
 649 ations in the shear-to-strain ratio of internal waves on inferred turbulent
 650 diffusivities. *Journal of Physical Oceanography*, *46*(11), 3299–3320. doi:
 651 10.1175/JPO-D-15-0161.1
- 652 Cimoli, L., Mashayek, A., Johnson, H. L., Marshall, D. P., Naveira Garabato, A. C.,
 653 Whalen, C. B., . . . MacKinnon, J. A. (2023). Significance of diapycnal mixing
 654 within the Atlantic meridional overturning circulation. *AGU Advances*, *4*(2),
 655 e2022AV000800.
- 656 Eriksen, C. C. (1985). Implications of Ocean Bottom Reflection for Internal Wave
 657 Spectra and Mixing. *Journal of Physical Oceanography*, *15*. doi: 10.1175/1520
 658 -0485(1985)015(1145:ioobrf)2.0.co;2
- 659 Eriksen, C. C. (1998). Internal wave reflection and mixing at Fieberling Guyot.
 660 *Journal of Geophysical Research: Oceans*, *103*. doi: 10.1029/97jc03205
- 661 Ganachaud, A., & Wunsch, C. (2000). Improved estimates of global ocean circula-
 662 tion, heat transport and mixing from hydrographic data. *Nature*. doi: 10.1038/
 663 35044048
- 664 Gargett, A. E. (1990). Do we really know how to scale the turbulent kinetic energy
 665 dissipation rate ϵ due to breaking of oceanic internal waves? *Journal of Geo-*
 666 *physical Research*, *95*(C9), 15971–15974. doi: 10.1029/jc095ic09p15971
- 667 Gargett, A. E., Hendricks, P. J., Sanford, T. B., Osborn, T. R., & Williams, A. J.
 668 (1981). A Composite Spectrum of Vertical Shear in the Upper Ocean. *Jour-*
 669 *nal of Physical Oceanography*, *11*. doi: 10.1175/1520-0485(1981)011(1258:
 670 acsovs)2.0.co;2
- 671 Garrett, C., & Munk, W. (1972). Space-Time scales of internal waves. *Geophysical*
 672 *Fluid Dynamics*, *3*(3), 225–264. doi: 10.1080/03091927208236082

- 673 Garrett, C., & Munk, W. (1975). Space-time scales of internal waves: A progress re-
674 port. *Journal of Geophysical Research*, *80*. doi: 10.1029/jc080i003p00291
- 675 Garrett, C., & Munk, W. (1979). Internal Waves in the Ocean. *Annual Review of*
676 *Fluid Mechanics*, *11*. doi: 10.1146/annurev.fl.11.010179.002011
- 677 Giglio, D., Lyubchich, V., & Mazloff, M. R. (2018). Estimating Oxygen in the
678 Southern Ocean Using Argo Temperature and Salinity. *Journal of Geophysical*
679 *Research: Oceans*, *123*(6), 4280–4297. doi: 10.1029/2017JC013404
- 680 Gregg, M. C. (1989). Scaling turbulent dissipation in the thermocline. *Journal of*
681 *Geophysical Research*, *94*(C7), 9686–9698. doi: 10.1029/jc094ic07p09686
- 682 Gregg, M. C. (1999). Uncertainties and limitations in measuring ϵ and $\chi(T)$. *Jour-*
683 *nal of Atmospheric and Oceanic Technology*, *16*, 1483–1490. doi: 10.1175/1520
684 -0426(1999)016<1483:ualima>2.0.co;2
- 685 Gregg, M. C., & Kunze, E. (1991). Shear and strain in Santa Monica Basin. *Jour-*
686 *nal of Geophysical Research: Oceans*, *96*(C9), 16709–16719. Retrieved from
687 <http://dx.doi.org/10.1029/91JC01385> doi: 10.1029/91JC01385
- 688 Gregg, M. C., Sanford, T. B., & Winkel, D. P. (2003). Reduced mixing
689 from the breaking of internal waves in equatorial waters. *Nature*. doi:
690 10.1038/nature01507
- 691 Gregg, M. C., Winkel, D. P., & Sanford, T. B. (1993). Varieties of fully resolved
692 spectra of vertical shear. *Journal of Physical Oceanography*, *23*. doi: 10.1175/
693 1520-0485(1993)023<0124:VOFRSO>2.0.CO;2
- 694 Henyey, F. S., Wright, J., & Flatté, S. M. (1986). Energy and action flow through
695 the internal wave field: An eikonal approach. *Journal of Geophysical Research*,
696 *91*. doi: 10.1029/jc091ic07p08487
- 697 Itsweire, E. C., Koseff, J. R., Briggs, D. A., & Ferziger, J. H. (1993). Turbulence
698 in stratified shear flows: implications for interpreting shear-induced mix-
699 ing in the ocean. *Journal of Physical Oceanography*, *23*, 1508–1522. doi:
700 10.1175/1520-0485(1993)023<1508:TISSFI>2.0.CO;2
- 701 Ivezić, Z., Connolly, A., Vanderplas, J., & Gray, A. (2014). *Statistics, data mining,*
702 *and machine learning in astronomy: a practical Python guide for the analysis*
703 *of survey data*. doi: 10.5860/choice.52-0257
- 704 Jackett, D. R., & McDougall, T. J. (1997). A neutral density variable for the world’s
705 oceans. *Journal of Physical Oceanography*, *27*(2), 237–263. doi: 10.1175/1520
706 -0485(1997)027<0237:ANDVFT>2.0.CO;2
- 707 Jeff A. Bilmes. (1998). A Gentle Tutorial of the EM Algorithm. *International Com-*
708 *puter Science Institute*, *4*(510).
- 709 Johnson, C. W., Ben-Zion, Y., Meng, H., & Vernon, F. (2020). Identifying Different
710 Classes of Seismic Noise Signals Using Unsupervised Learning. *Geophysical Re-*
711 *search Letters*, *47*(15), 1–10. doi: 10.1029/2020GL088353
- 712 Johnston, T. M., & Rudnick, D. L. (2015). Trapped diurnal internal tides, prop-
713 agating semidiurnal internal tides, and mixing estimates in the Califor-
714 nia Current System from sustained glider observations, 2006-2012. *Deep-*
715 *Sea Research Part II: Topical Studies in Oceanography*, *112*, 61–78. doi:
716 10.1016/j.dsr2.2014.03.009
- 717 Jones, D. C., Holt, H. J., Meijers, A. J., & Shuckburgh, E. (2019). Unsupervised
718 Clustering of Southern Ocean Argo Float Temperature Profiles. *Journal of*
719 *Geophysical Research: Oceans*, *124*(1), 390–402. doi: 10.1029/2018JC014629
- 720 Kaiser, B. E., Saenz, J. A., Sonnewald, M., & Livescu, D. (2022). Automated iden-
721 tification of dominant physical processes. *Engineering Applications of Artificial*
722 *Intelligence*, *116*, 105496.
- 723 Klymak, J. M., Pinkel, R., & Rainville, L. (2008). Direct Breaking of the Internal
724 Tide near Topography: Kaena Ridge, Hawaii. *Journal of Physical Oceanogra-*
725 *phy*, *38*, 380–399. doi: 10.1175/2007JPO3728.1
- 726 Konishi, S., Ando, T., & Imoto, S. (2004). Bayesian information criteria and
727 smoothing parameter selection in radial basis function networks. *Biometrika*,

- 728 91(1). doi: 10.1093/biomet/91.1.27
- 729 Kunze, E. (2017a). The Internal-Wave-Driven Meridional Overturning Circulation.
730 *Journal of Physical Oceanography*, 47(11), 2673–2689. doi: 10.1175/JPO-D-16
731 -0142.1
- 732 Kunze, E. (2017b). Internal-Wave-Driven Mixing: Global Geography and Budgets.
733 *Journal of Physical Oceanography*, 47(6), 1325–1345. Retrieved from [http://](http://journals.ametsoc.org/doi/10.1175/JPO-D-16-0141.1)
734 journals.ametsoc.org/doi/10.1175/JPO-D-16-0141.1 doi: 10.1175/JPO-D
735 -16-0141.1
- 736 Kunze, E., Firing, E., Hummon, J. M., Chereskin, T. K., & Thurnherr, A. M.
737 (2006). Global abyssal mixing inferred from lowered ADCP shear and CTD
738 strain profiles. *Journal of Physical Oceanography*, 36(8), 1553–1576. doi:
739 10.1175/JPO2926.1
- 740 Kunze, E., Rosenfeld, L. K., Carter, G. S., & Gregg, M. C. (2002). Internal waves in
741 Monterey Submarine Canyon. *Journal of Physical Oceanography*, 32. doi: 10
742 .1175/1520-0485(2002)032<1890:IWIMSC>2.0.CO;2
- 743 Lee, D. D., & Seung, H. S. (1999). Learning the parts of objects by non-negative
744 matrix factorization. *Nature*, 401, 788–791. doi: 10.1038/44565
- 745 Lele, R., Purkey, S. G., Nash, J. D., Mackinnon, J. A., Thurnherr, A. M., Whalen,
746 C. B., ... Talley, L. D. (2021). Abyssal Heat Budget in the Southwest Pa-
747 cific Basin. *Journal of Physical Oceanography*, 51(11), 3317–3333. doi:
748 10.1175/JPO-D-21-0045.1
- 749 MacKinnon, J. A., & Gregg, M. C. (2003). Mixing on the Late-Summer New Eng-
750 land Shelf—Solibores, Shear, and Stratification. *Journal of Physical Oceanog-*
751 *raphy*, 35(12), 2408–2424. doi: 10.1175/1520-0485(2003)033<1476:motlne>2.0
752 .co;2
- 753 MacKinnon, J. A., Zhao, Z., Whalen, C. B., Waterhouse, A. F., Trossman, D. S.,
754 Sun, O. M., ... Alford, M. H. (2017). Climate process team on internal wave-
755 driven ocean mixing. *Bulletin of the American Meteorological Society*, 98(11),
756 2429–2454. doi: 10.1175/BAMS-D-16-0030.1
- 757 Mashayek, A., Reynard, N., Zhai, F., Srinivasan, K., Jelley, A., Naveira Garabato,
758 A., & Caulfield, C. P. (2022). Deep ocean learning of small scale turbulence.
759 *Geophysical Research Letters*, 49(15), e2022GL098039.
- 760 Maze, G., Mercier, H., Fablet, R., Tandeo, P., Lopez Radcenco, M., Lenca, P., ...
761 Le Goff, C. (2017). Coherent heat patterns revealed by unsupervised classifi-
762 cation of Argo temperature profiles in the North Atlantic Ocean. *Progress in*
763 *Oceanography*, 151. doi: 10.1016/j.pocean.2016.12.008
- 764 McDougall, P., Trevor J. ; Barker. (2011). Getting started with TEOS-10 and the
765 Gibbs Seawater (GSW) Oceanographic Toolbox. *Scor/Iapso Wg127*.
- 766 Moum, J. N., & Nash, J. D. (2009). Mixing Measurements on an Equatorial Ocean
767 Mooring. *Journal of Atmospheric and Oceanic Technology*, 26(2), 317–336.
768 doi: 10.1175/2008JTECHO617.1
- 769 Müller, P., & Liu, X. (2000). Scattering of internal waves at finite topography in
770 two dimensions. Part I: Theory and case studies. *Journal of Physical Oceanog-*
771 *raphy*, 30, 532–549. doi: 10.1175/1520-0485(2000)030<0532:SOIWAF>2.0.CO;
772 2
- 773 Munk, W. (1981). Internal Waves and Small-Scale Processes. In *Evolution of physi-*
774 *cal oceanography: Scientific surveys in honor of henry stommel*.
- 775 Munk, W. H. (1966). Abyssal recipes. *Deep-Sea Research and Oceanographic Ab-*
776 *stracts*. doi: 10.1016/0011-7471(66)90602-4
- 777 Naveira Garabato, A. C., Frajka-Williams, E. E., Spingys, C. P., Legg, S., Polzin,
778 K. L., Forryan, A., ... Meredith, M. P. (2019). Rapid mixing and exchange of
779 deep-ocean waters in an abyssal boundary current. *Proceedings of the National*
780 *Academy of Sciences of the United States of America*, 116(27), 13233–13238.
781 doi: 10.1073/pnas.1904087116
- 782 Naveira Garabato, A. C., Polzin, K. L., King, B. A., Heywood, K. J., & Visbeck, M.

- 783 (2004). Widespread Intense Turbulent Mixing in the Southern Ocean. *Science*,
784 *303*, 210–213. doi: 10.1126/science.1090929
- 785 Oakey, N. S. (1982). Determination of the Rate of Dissipation of Turbulent
786 Energy from Simultaneous Temperature and Velocity Shear Microstruc-
787 ture Measurements. *Journal of Physical Oceanography*, *12*, 256–271. doi:
788 10.1175/1520-0485(1982)012<0256:dotrod>2.0.co;2
- 789 Osborn, T. R. (1980). Estimates of the Local Rate of Vertical Diffusion from Dissi-
790 pation Measurements. *Journal of Physical Oceanography*, *10*(1), 83–89. doi: 10
791 .1175/1520-0485(1980)010{\%}3C0083:EOTLRO{\%}3E2.0.CO;2
- 792 Osborn, T. R., & Cox, C. S. (1972). Oceanic fine structure. *Geophysical & Astro-
793 physical Fluid Dynamics*, *3*(4), 321–345. doi: 10.1080/03091927208236085
- 794 Pedregosa, F., Varoquaux, G., Gramfort, A., Michel, V., Thirion, B., Grisel, O., ...
795 Duchesnay, (2011). Scikit-learn: Machine learning in Python. *Journal of
796 Machine Learning Research*, *12*, 2825–2830.
- 797 Pollmann, F. (2020). Global characterization of the ocean’s internal wave spectrum.
798 *Journal of Physical Oceanography*, *50*(7), 1871–1891. doi: 10.1175/JPO-D-19
799 -0185.1
- 800 Polzin, K., & Ferrari, R. (2004). Isopycnal dispersion in NATRE. *Journal of Physi-
801 cal Oceanography*, *34*. doi: 10.1175/1520-0485(2004)034<0247:IDIN>2.0.CO;2
- 802 Polzin, K., Kunze, E., Toole, J. M., & Schmitt, R. W. (2003). The partition of
803 finescale energy into internal waves and subinertial motions. *Journal of Physi-
804 cal Oceanography*, *33*. doi: 10.1175/1520-0485(2003)033<0234:TPOFEI>2.0.CO;
805 2
- 806 Polzin, K. L., & Lvov, Y. (2011). Towards Regional Characterization of the Oceanic
807 Internal Wavefield. *Reviews of Geophysics*, *49*. doi: 10.1029/2010RG000329
- 808 Polzin, K. L., Naveira Garabato, A. C., Huussen, T. N., Sloyan, B. M., & Wa-
809 terman, S. (2014). Finescale parameterizations of turbulent dissipa-
810 tion. *Journal of Geophysical Research: Oceans*, *119*(2), 1383–1419. doi:
811 10.1002/2013JC008979
- 812 Polzin, K. L., Toole, J. M., Ledwell, J. R., & Schmitt, R. W. (1997). Spatial vari-
813 ability of turbulent mixing in the abyssal ocean. *Science*, *276*(5309), 93–96.
814 doi: 10.1126/science.276.5309.93
- 815 Polzin, K. L., Toole, J. M., & Schmitt, R. W. (1995). Finescale Parameterizations of
816 Turbulent Dissipation. *Journal of Physical Oceanography*, *25*(3), 306–328. doi:
817 https://doi.org/10.1175/1520-0485(1995)025<0306:FPOTD>2.0.CO;2
- 818 Rosso, I., Mazloff, M. R., Talley, L. D., Purkey, S. G., Freeman, N. M., & Maze,
819 G. (2020). Water Mass and Biogeochemical Variability in the Kerguelen
820 Sector of the Southern Ocean: A Machine Learning Approach for a Mixing
821 Hot Spot. *Journal of Geophysical Research: Oceans*, *125*(3), 1–23. doi:
822 10.1029/2019JC015877
- 823 Rousseeuw, P. J. (1987). Silhouettes: A graphical aid to the interpretation and vali-
824 dation of cluster analysis. *Journal of Computational and Applied Mathematics*,
825 *20*, 53–65. doi: 10.1016/0377-0427(87)90125-7
- 826 Rudnick, D. L., Johnston, T. M., & Sherman, J. T. (2013). High-frequency internal
827 waves near the Luzon Strait observed by underwater gliders. *Journal of Geo-
828 physical Research: Oceans*, *118*. doi: 10.1002/jgrc.20083
- 829 Schwarz G. (1978). Estimating the dimension of a model. *The annals of statistics*,
830 *6*(2).
- 831 Shroyer, E. L., Rudnick, D. L., Farrar, J. T., Lim, B., Venayagamoorthy, S. K., Lau-
832 rent, L. C., ... Moum, J. N. (2016). Modification of upper-ocean temperature
833 structure by subsurface mixing in the presence of strong salinity stratification.
834 *Oceanography*, *29*(2), 62–71. doi: 10.5670/oceanog.2016.39
- 835 Sonnewald, M., Sonnewald, M., Dutkiewicz, S., Hill, C., & Forget, G. (2020). Eluci-
836 dating ecological complexity: Unsupervised learning determines global marine
837 eco-provinces. *Science Advances*, *6*(22). doi: 10.1126/sciadv.aay4740

- 838 Sonnewald, M., Wunsch, C., & Heimbach, P. (2019). Unsupervised Learning Reveals
839 Geography of Global Ocean Dynamical Regions. *Earth and Space Science*, *6*.
840 doi: 10.1029/2018EA000519
- 841 St. Laurent, L., Naveira Garabato, A. C., Ledwell, J. R., Thurnherr, A. M.,
842 Toole, J. M., & Watson, A. J. (2012). Turbulence and diapycnal mixing
843 in drake passage. *Journal of Physical Oceanography*, *42*, 2143–2152. doi:
844 10.1175/JPO-D-12-027.1
- 845 Talley, L. D. (2003). Shallow, Intermediate, and Deep Overturning Components of
846 the Global Heat Budget. *Journal of Physical Oceanography*. doi: 10.1175/1520
847 -0485(2003)033<0530:siadoc>2.0.co;2
- 848 Thurnherr, A. M., Visbeck, M., Firing, E., King, B. A., Hummon, J., Krahnemann, G.,
849 & Huber, B. A. (2010). A Manual For Acquiring Lowered Doppler Current
850 Profiler Data. *The GO-SHIP Repeat Hydrographic Manual: A Collection of*
851 *Expert Reports and Guidelines*, *14*(134).
- 852 Visbeck, M. (2002). Deep velocity profiling using lowered acoustic Doppler cur-
853 rent profilers: Bottom track and inverse solutions. *Journal of Atmospheric and*
854 *Oceanic Technology*, *19*(5), 794–807. doi: 10.1175/1520-0426(2002)019<0794:
855 DVPULA>2.0.CO;2
- 856 Waterhouse, A. F., Mackinnon, J. A., Nash, J. D., Alford, M. H., Kunze, E., Sim-
857 mons, H. L., . . . Lee, C. M. (2014). Global patterns of diapycnal mixing from
858 measurements of the turbulent dissipation rate. *Journal of Physical Oceanogra-*
859 *phy*, *44*(7), 1854–1872. doi: 10.1175/JPO-D-13-0104.1
- 860 Waterman, S., Naveira Garabato, A. C., & Polzin, K. L. (2013). Internal waves and
861 turbulence in the antarctic circumpolar current. *Journal of Physical Oceanog-*
862 *raphy*, *43*(2), 259–282. doi: 10.1175/JPO-D-11-0194.1
- 863 Waterman, S., Polzin, K. L., Garabato, A. C., Sheen, K. L., & Forryan, A. (2014).
864 Suppression of internal wave breaking in the antarctic circumpolar current
865 near topography. *Journal of Physical Oceanography*, *44*(5), 1466–1492. doi:
866 10.1175/JPO-D-12-0154.1
- 867 Waterman, S., Polzin, K. L., Naveira Garabato, A. C., Sheen, K. L., & Forryan,
868 A. (2014). Suppression of Internal Wave Breaking in the Antarctic Circum-
869 polar Current near Topography. *Journal of Physical Oceanography*, *44*(5),
870 1466–1492. doi: 10.1175/JPO-D-12-0154.1
- 871 Whalen, C. B. (2021). Best Practices for Comparing Ocean Turbulence Measure-
872 ments Across Spatiotemporal Scales. *Journal of Atmospheric & Oceanic Tech-*
873 *nology*, *38*(4), 837–841. doi: <https://doi.org/10.1175/JTECH-D-20-0175.1>
- 874 Whalen, C. B., MacKinnon, J. A., & Talley, L. D. (2018). Large-scale impacts of
875 the mesoscale environment on mixing from wind-driven internal waves. *Nature*
876 *Geoscience*, *11*(11), 842–847. Retrieved from [http://dx.doi.org/10.1038/
877 s41561-018-0213-6](http://dx.doi.org/10.1038/s41561-018-0213-6) doi: 10.1038/s41561-018-0213-6
- 878 Whalen, C. B., MacKinnon, J. A., Talley, L. D., & Waterhouse, A. F. (2015).
879 Estimating the Mean Diapycnal Mixing Using a Finescale Strain Param-
880 eterization. *Journal of Physical Oceanography*, *45*(4), 1174–1188. doi:
881 10.1175/JPO-D-14-0167.1
- 882 Whalen, C. B., Talley, L. D., & MacKinnon, J. A. (2012). Spatial and temporal
883 variability of global ocean mixing inferred from Argo profiles. *Geophysical Re-*
884 *search Letters*, *39*(17), 1–6. doi: 10.1029/2012GL053196
- 885 Wunsch, C., & Ferrari, R. (2004). Vertical mixing, energy, and the general circula-
886 tion of the oceans. *Annual Review of Fluid Mechanics*, *36*(1), 281–314. doi: 10
887 .1146/annurev.fluid.36.050802.122121

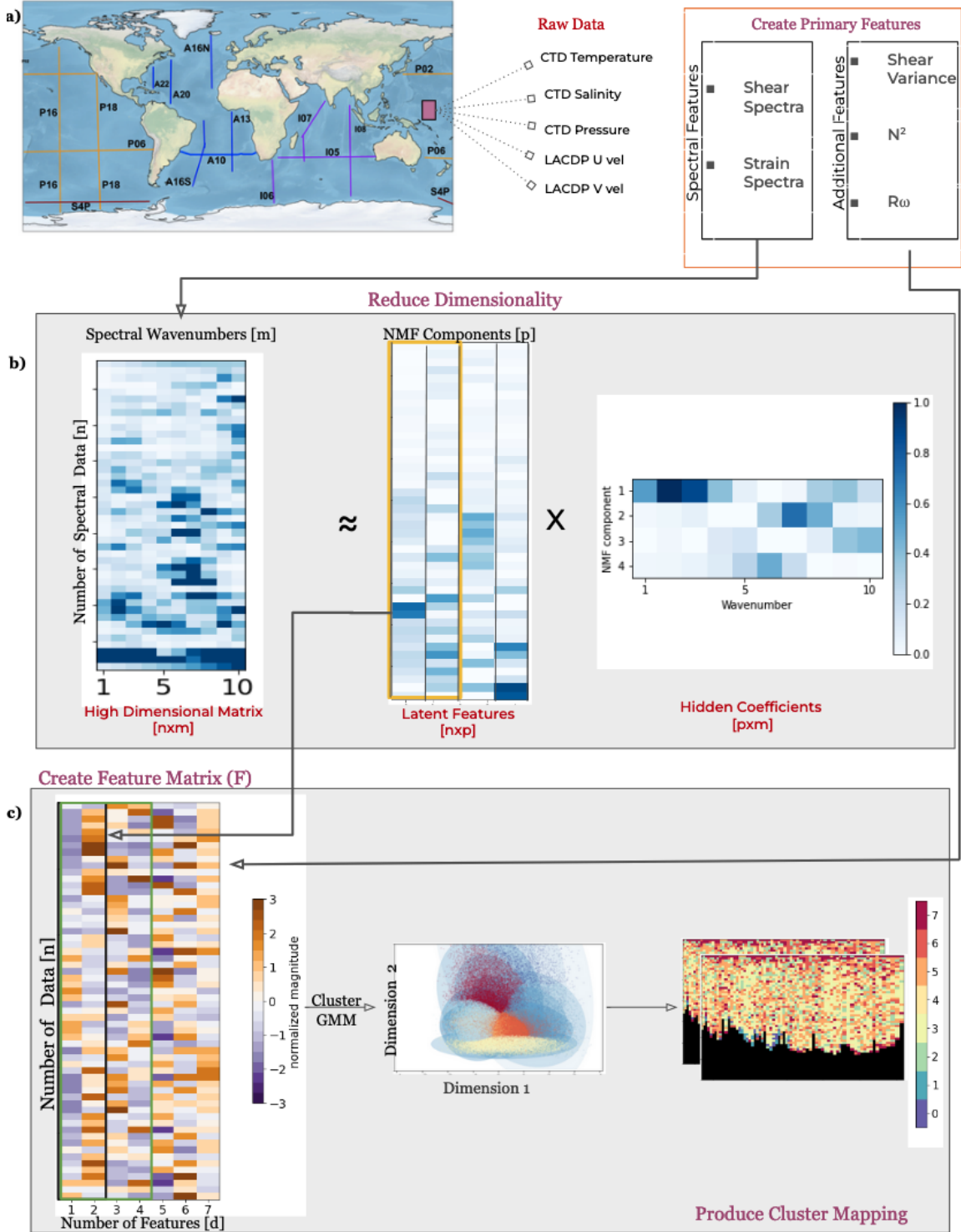


Figure 1. Method schematic shows the locations of the Raw CTD and LACDP data along the 15 GO-SHIP lines in the study which are used to create primary features consisting of spectral and non-spectral data (see Section 3.2). (b) An example showing dimensionality reduction through NMF decomposition for shear spectra, converting high m dimensional spectra in the input data matrix \mathbf{X} into lower p dimensional spectral features in the form of a latent feature matrix \mathbf{W} and a corresponding hidden coefficient matrix \mathbf{H} respectively (see Section 3.2.1). (c) Two latent spectral features each ($p=2$) of shear and strain are aggregated into a feature matrix \mathbf{F} (green box, see Section 3.2.2), with additional features (see Section 4.3) are used as inputs to the GMM model to generate cluster mappings for all GO-SHIP sections (Table 1).

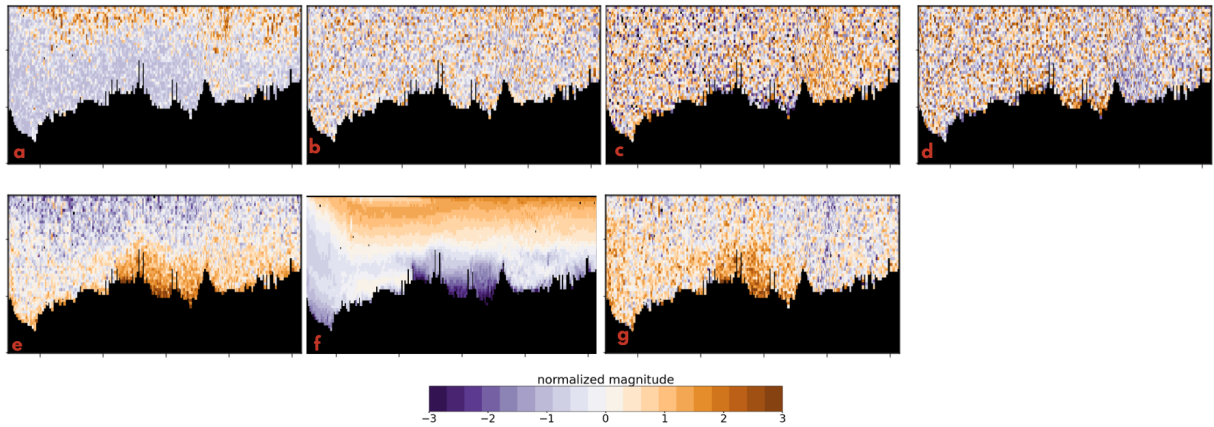


Figure 2. Example of geographical feature distribution along the P18 section for 7 different features with normalized magnitudes used for clustering using the GMM model including NMF-1 shear spectra (a), NMF-2 shear spectra (b), NMF-1 strain spectra (c), NMF-2 strain spectra (d), shear variance $\langle V_z^2 \rangle$ (e), buoyancy frequency [N] (f) and R_ω (g).

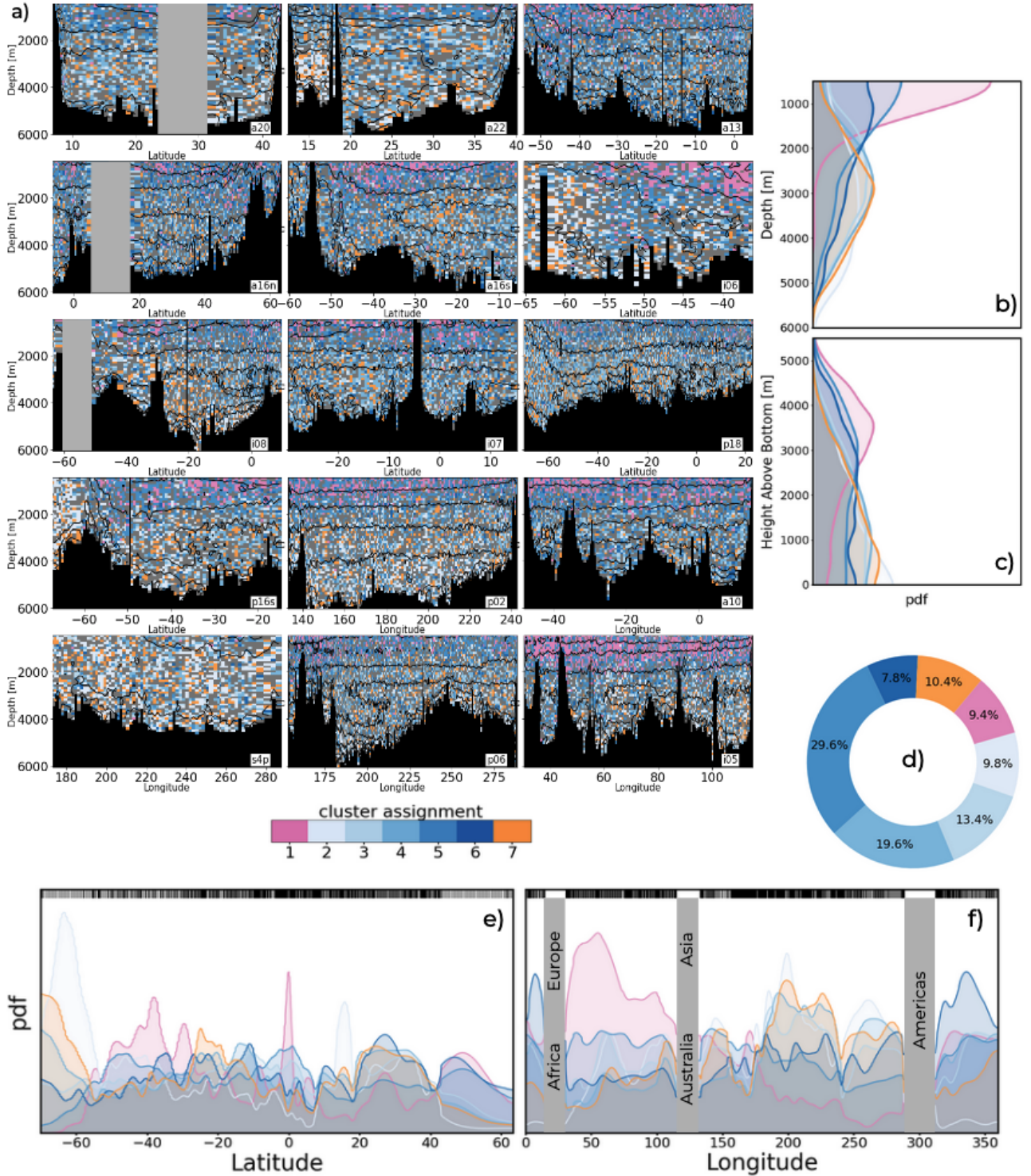


Figure 3. a) Resulting clustering along the 15 GO-SHIP lines produced by the GMM model with feature matrix based on the NMF features (Figure 2a-d). PDF showing the abundance and variation of individual clusters as a function of depth (b) and height above bottom bathymetry across all 15 GO-SHIP lines (c). Relative percentage distribution of the seven clusters from the GMM model with a posterior probability greater than 70% which are considered for the analysis (d). The zonal (e) and meridional (f) PDF computed from a composites of 10 zonal and 5 meridional sections respectively, with the location of CTD stations for the zonal and meridional sections are shown (black vertical lines in e and f).

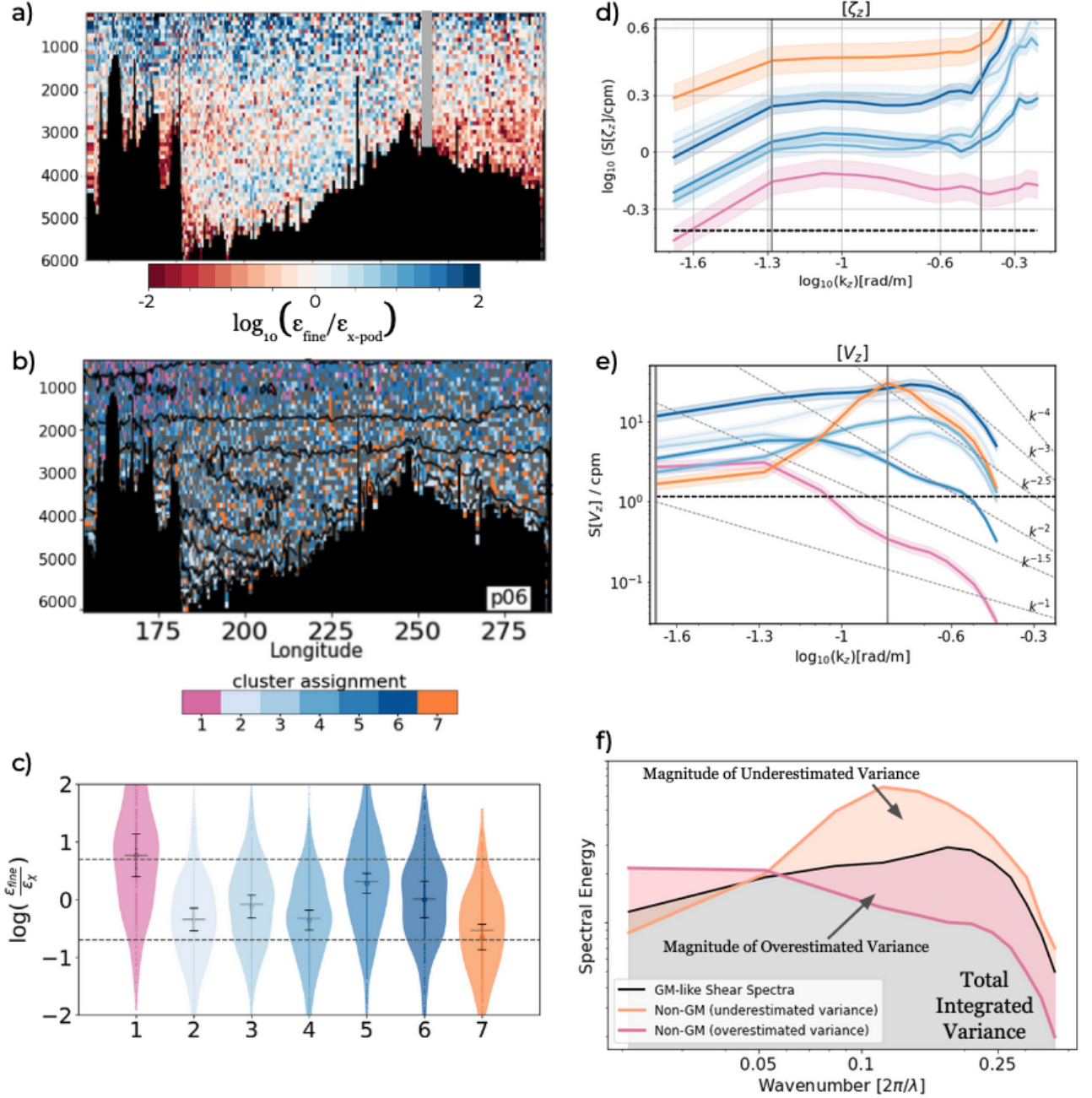


Figure 4. a) Ratio of estimates of turbulent dissipation rate from the finescale parameterization to measurements from CTD-mounted χ -pods taken concurrently along the P06 section expressed as $\log_{10}(\frac{\epsilon_{\text{fine}}}{\epsilon_{\text{x-pod}}})$, b) Cluster assignments from the GMM model along the P06 section (same as Figure 3a), c) Mean, 95% confidence intervals and violin plot computed for the ratio $\log_{10}(\frac{\epsilon_{\text{fine}}}{\epsilon_{\text{x-pod}}})$ from Figure 4a for seven clustered regions shown in Figure 4b, d-e). Mean strain and shear spectra computed as a composite average for the clusters computed using all 15 sections with 99% confidence intervals using computed using a χ^2 distribution (Chatfield et al., 1987) considering only $1/10^{\text{th}}$ degrees of freedom for better visibility (color shading). The average GM spectral levels are shown in the dashed black line, with the integration limits to calculate strain and shear variance shown by solid grey vertical lines. Slopes for shear spectra roll-offs between k^{-1} and k^{-4} are shown with high wavenumber asymptote k^{-2} representing inertial subrange in the GM model, f) Schematic outlining how biases in estimates of turbulent mixing could arise from spectra deviating from the assumed GM-like shape in the finescale parameterization (Equation 1) by either overestimating (Cluster 1) or underestimating (Cluster 7) shear $\langle V_z^2 \rangle$ and strain variance $\langle \zeta_z^2 \rangle$ calculated by integrating the respective spectra in the finescale wavenumber band.

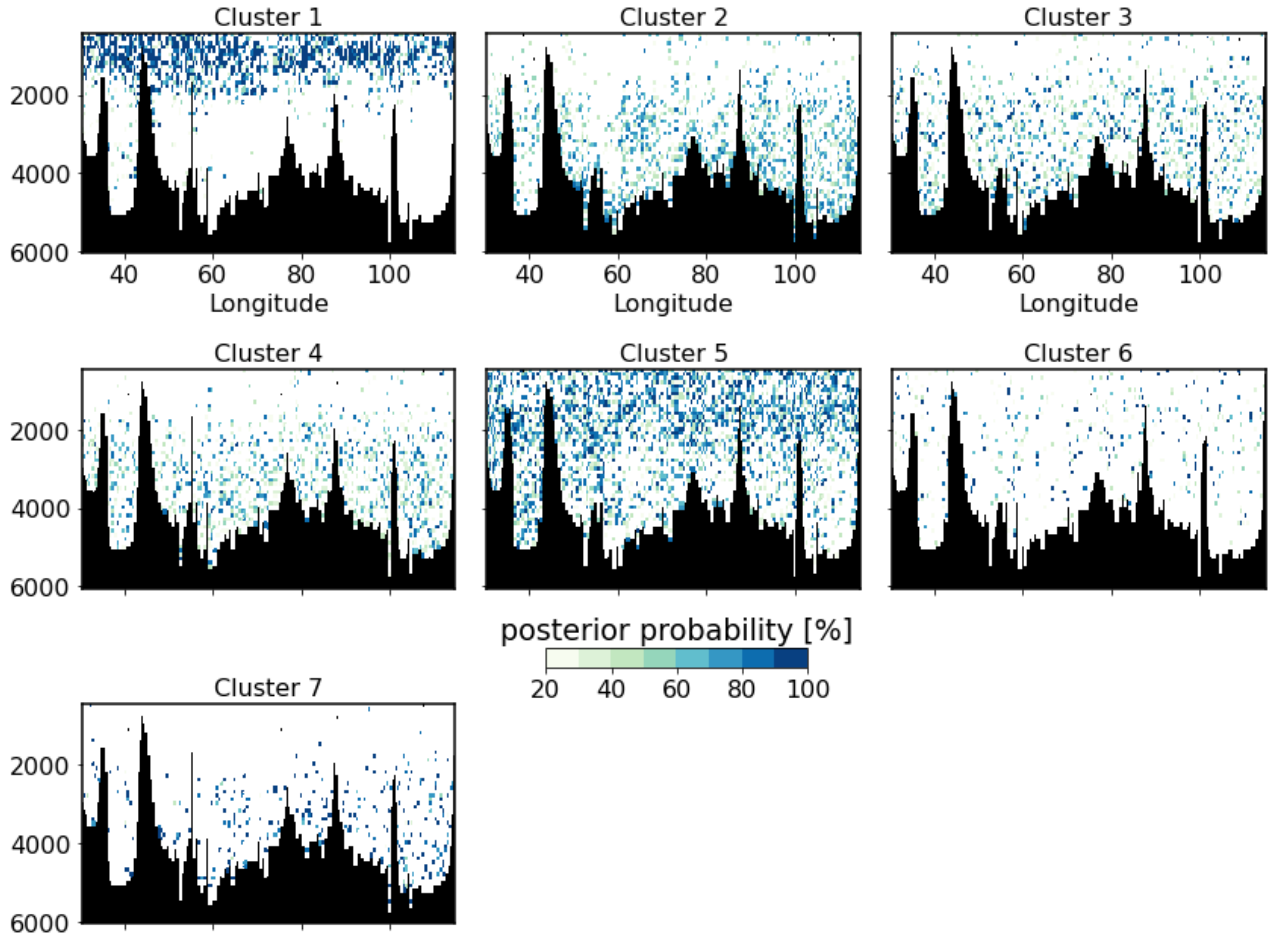


Figure 5. Posterior probabilities (%) $p(k|x)$ of data belonging to each of the clusters (1-7) as calculated with Equation 6 from the GMM model along the I05 section. Final cluster assignment of a data point belonging to a cluster k as shown in Figure 4 is made by computing $k = \operatorname{argmax}_x p(k|x)$ as described in Section 3.3 .

I05

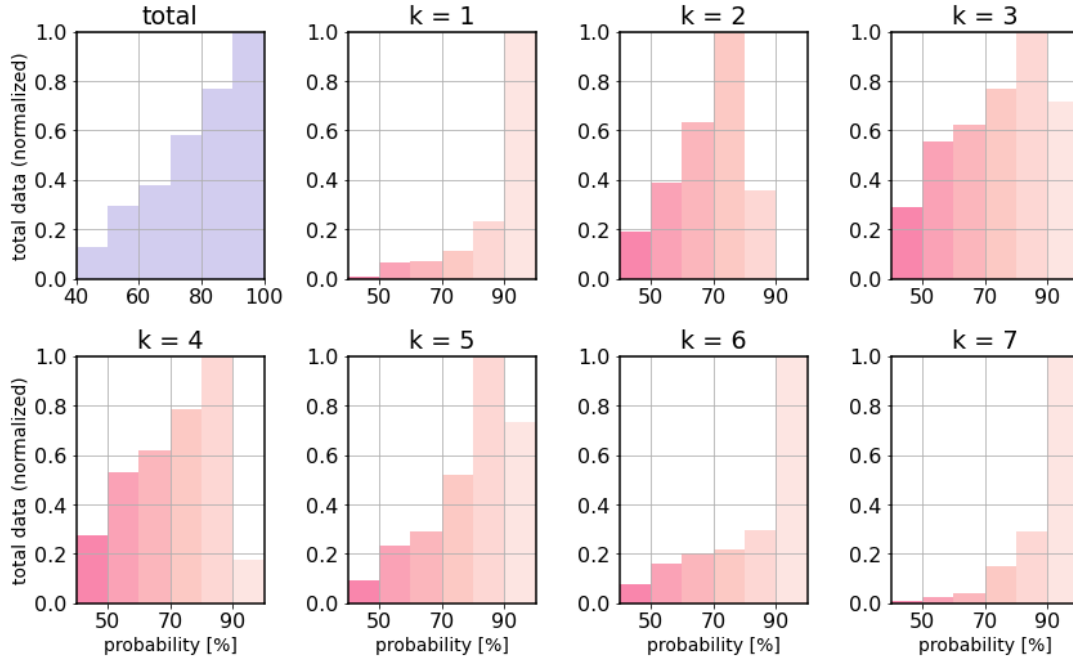


Figure 6. Histogram of the total percent posterior probabilities along the I05 section summed across all the clusters $\sum_{k=1}^K p(k|x)$ in 10% bins between 40% to 100% (top left). Additionally, histogram of the percent posterior probabilities in each individual clusters $k=1-7$ corresponding to Figure 5 are displayed as well. Data displayed in each bin are normalized by number of data-points in the 10% bin with the most data.

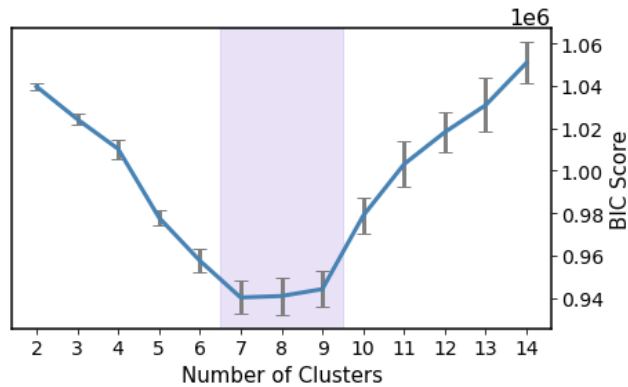


Figure 7. The BIC scores versus the specified number of clusters, with the means (solid blue line) and standard deviations (error bars) calculated from 50 random subsets of the data is also shown with the range of the smallest BIC values (between $k=7$ and $k=9$) is indicated (purple shading)

Figure 1.

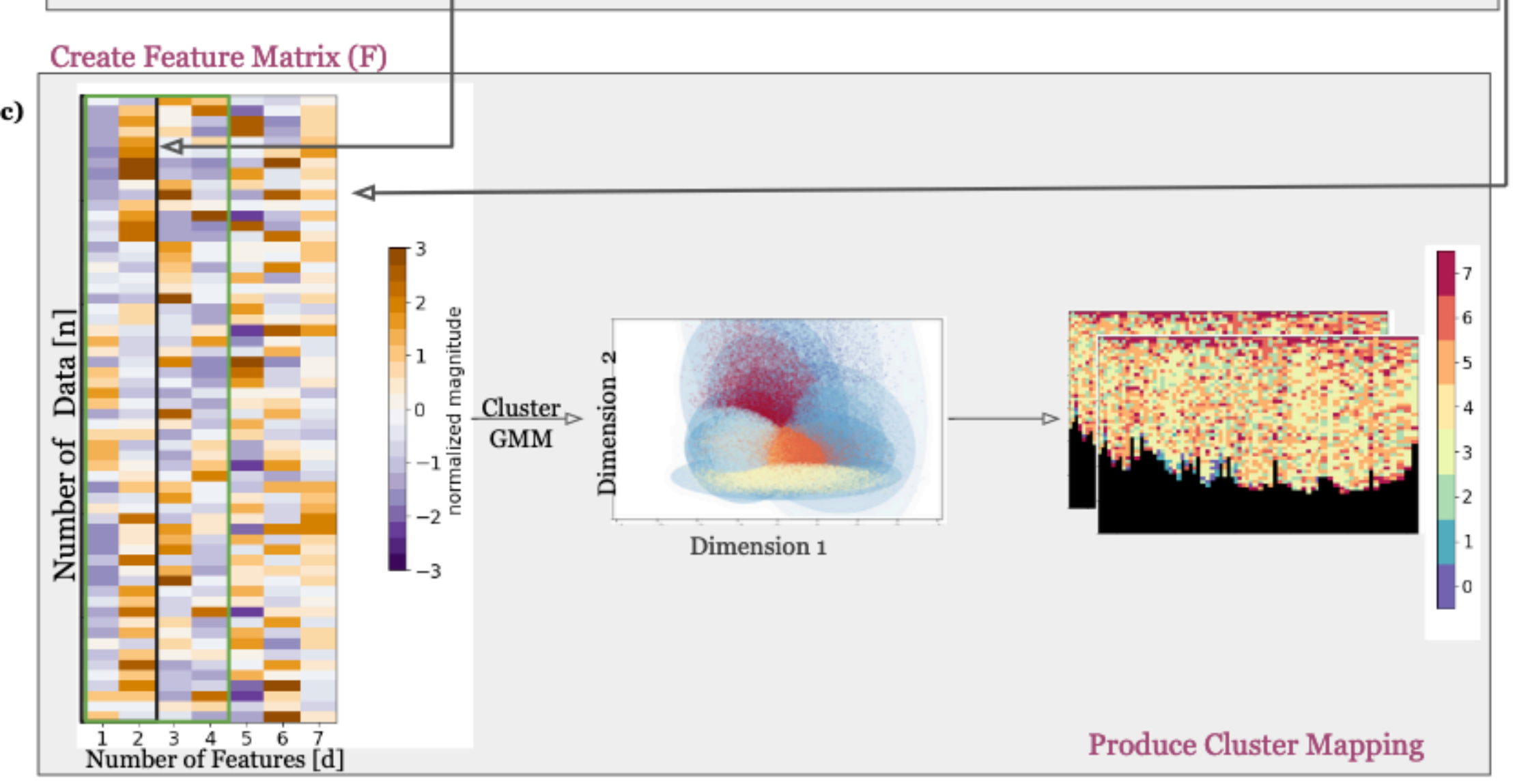
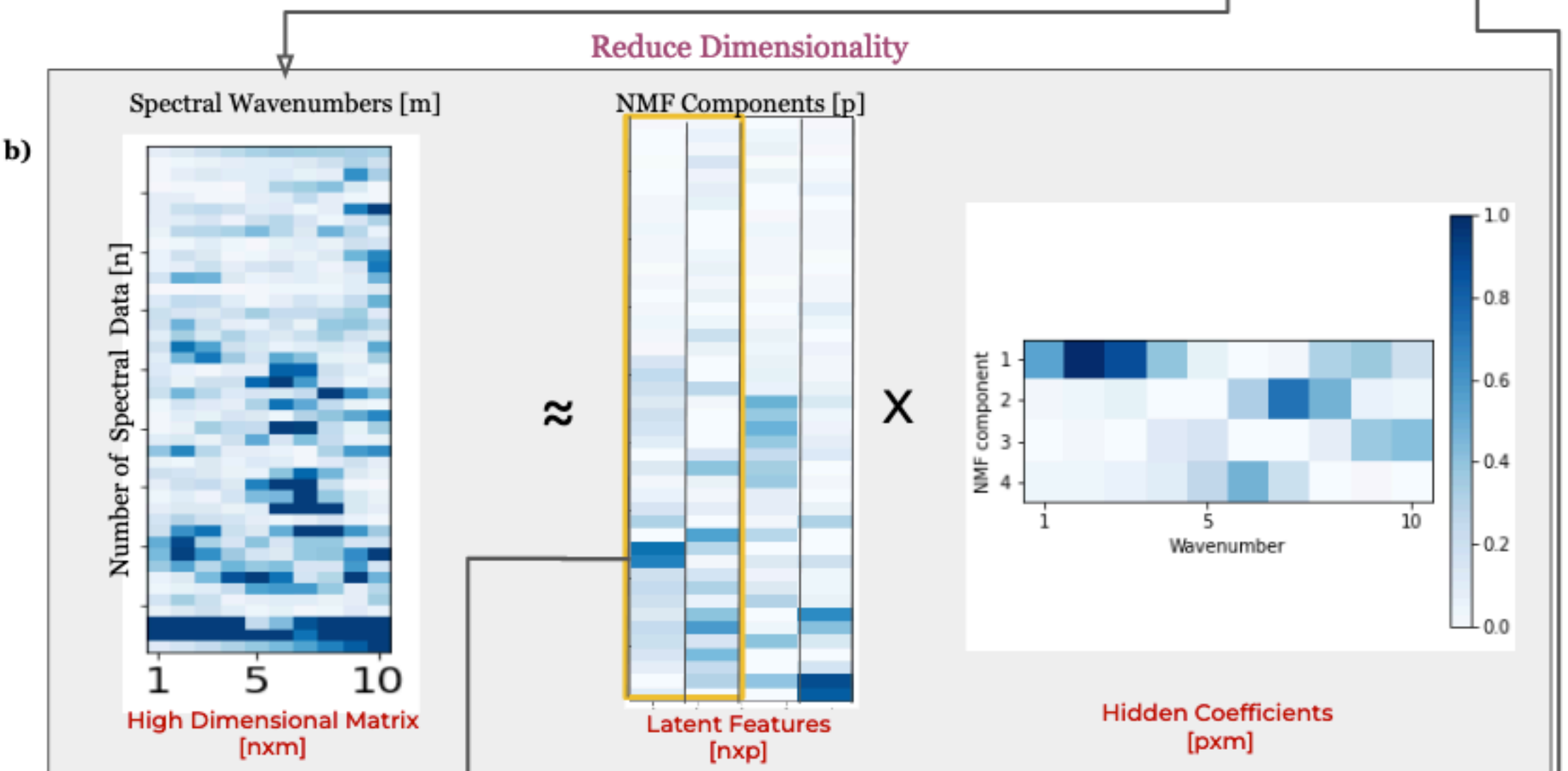
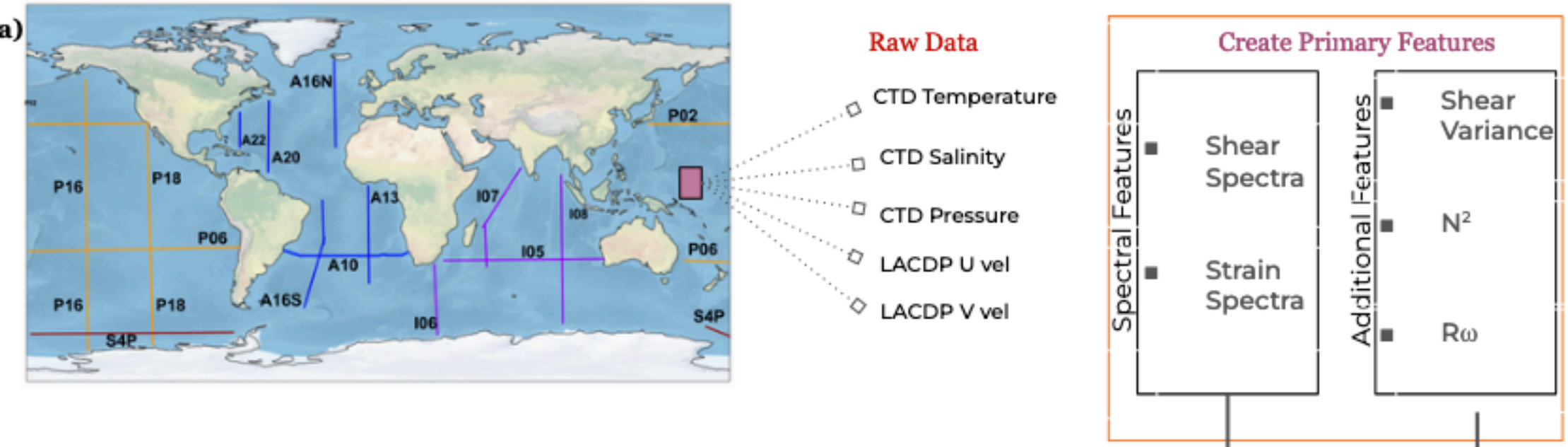


Figure 2.

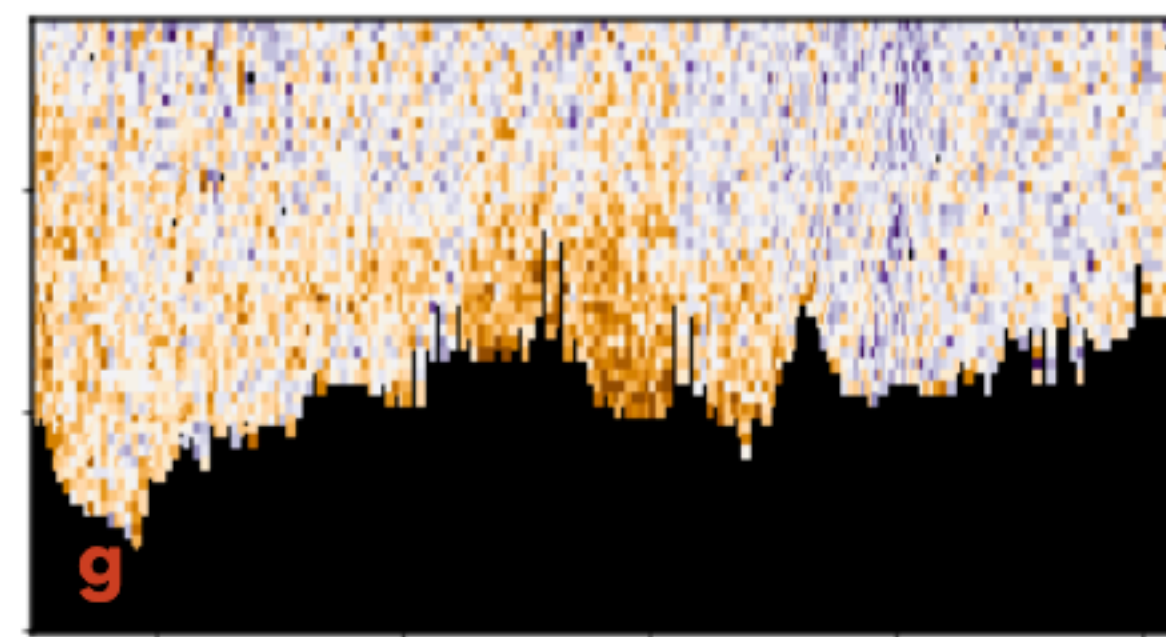
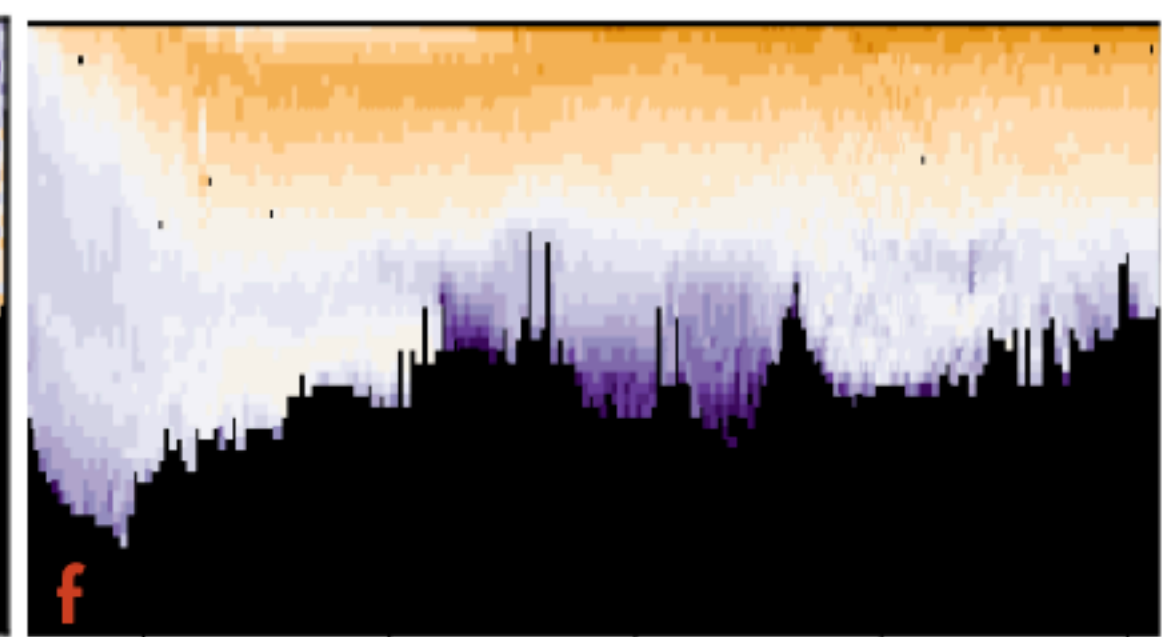
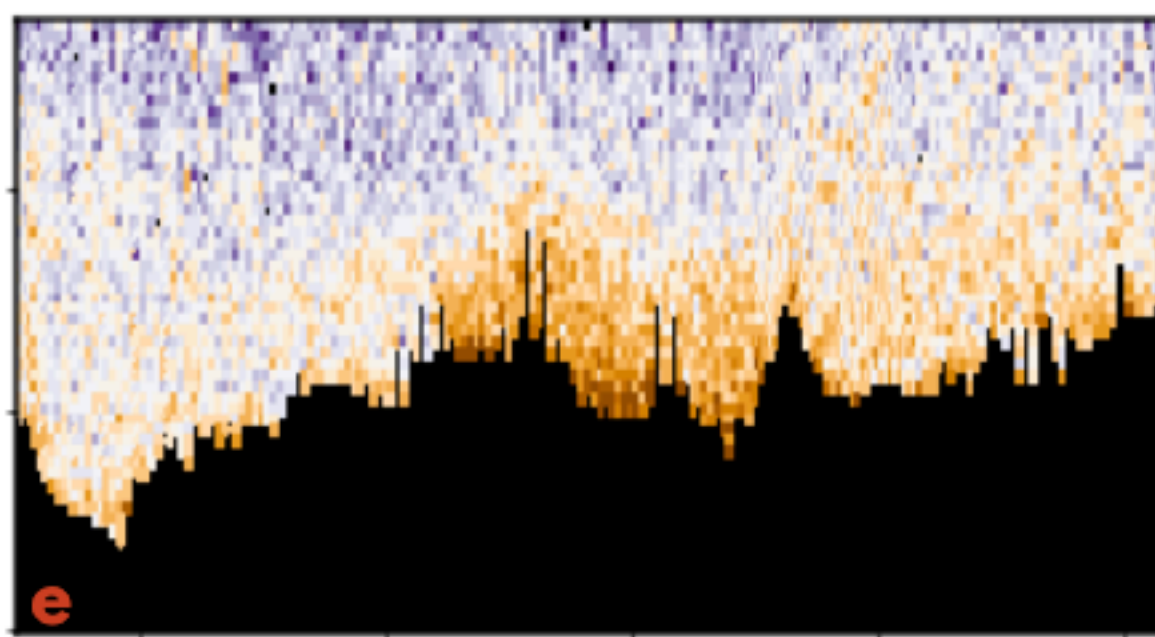
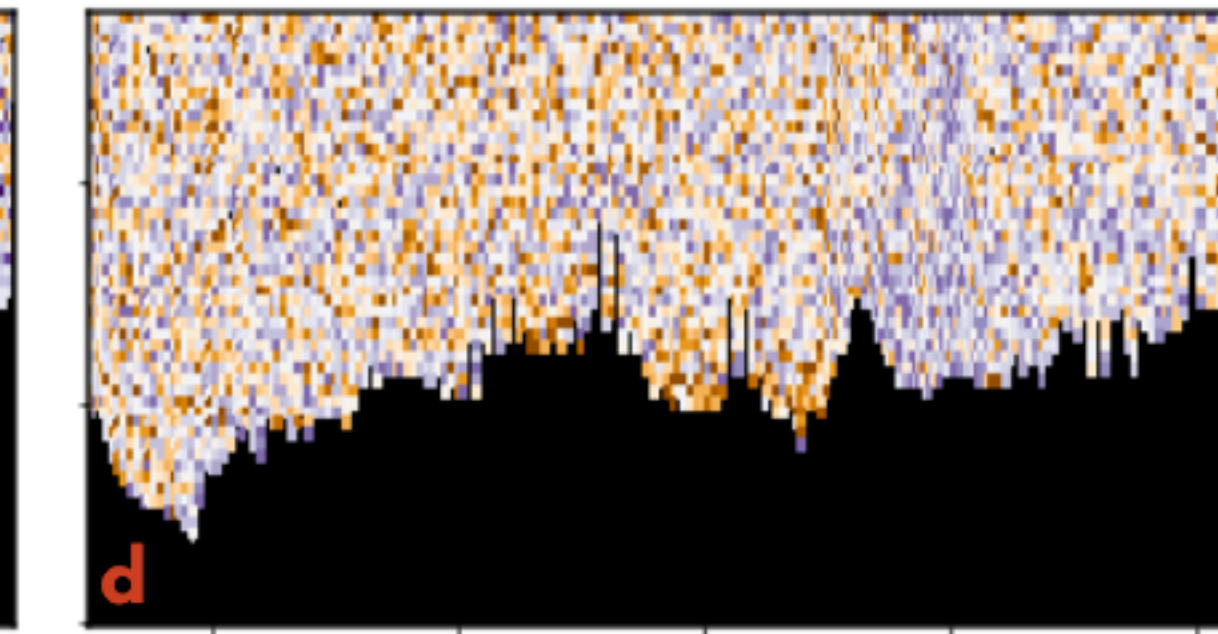
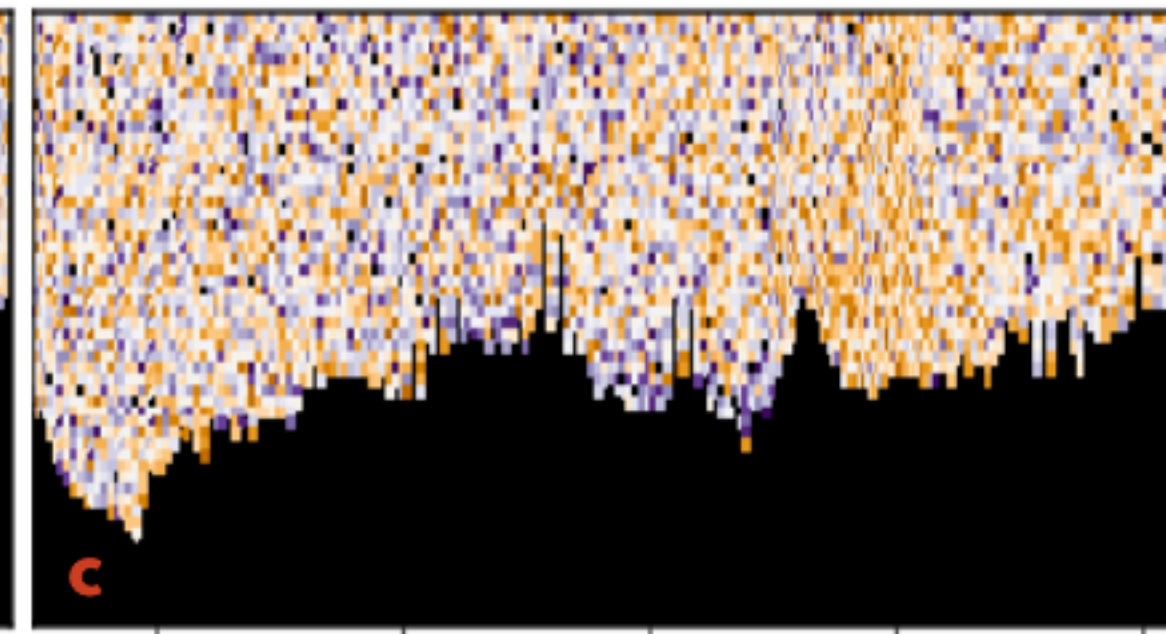
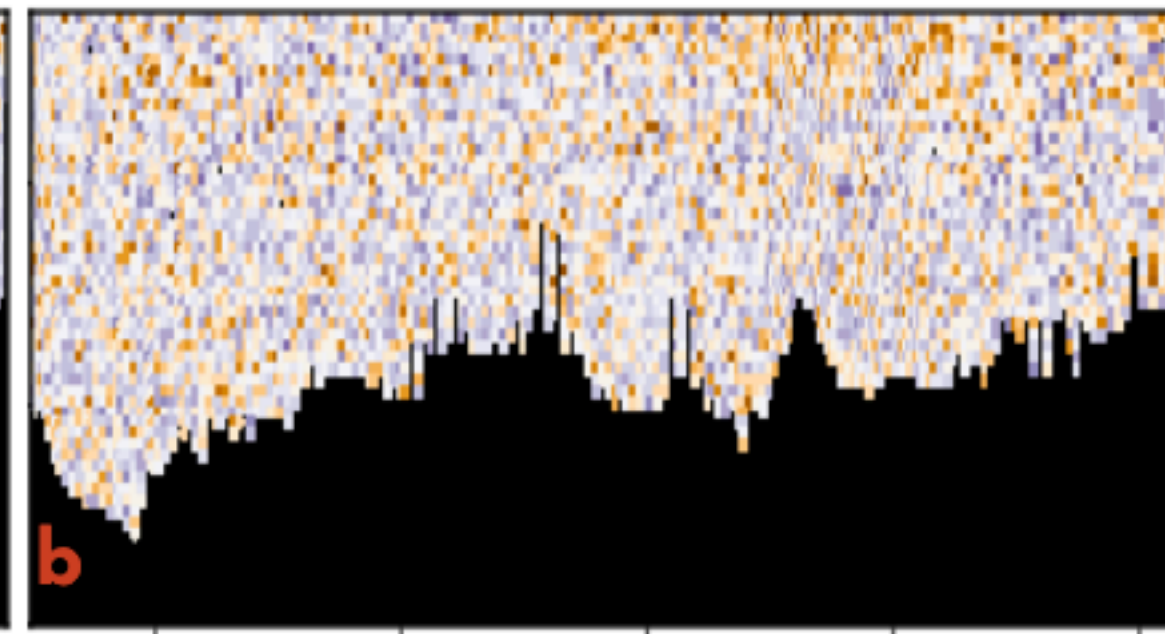
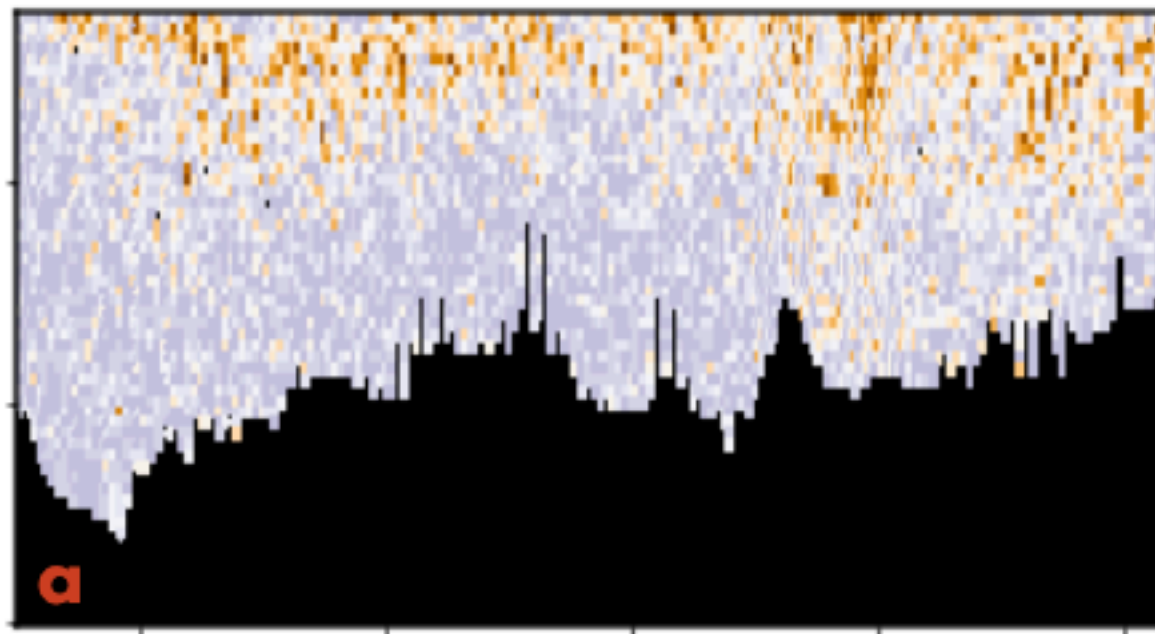


Figure 3.

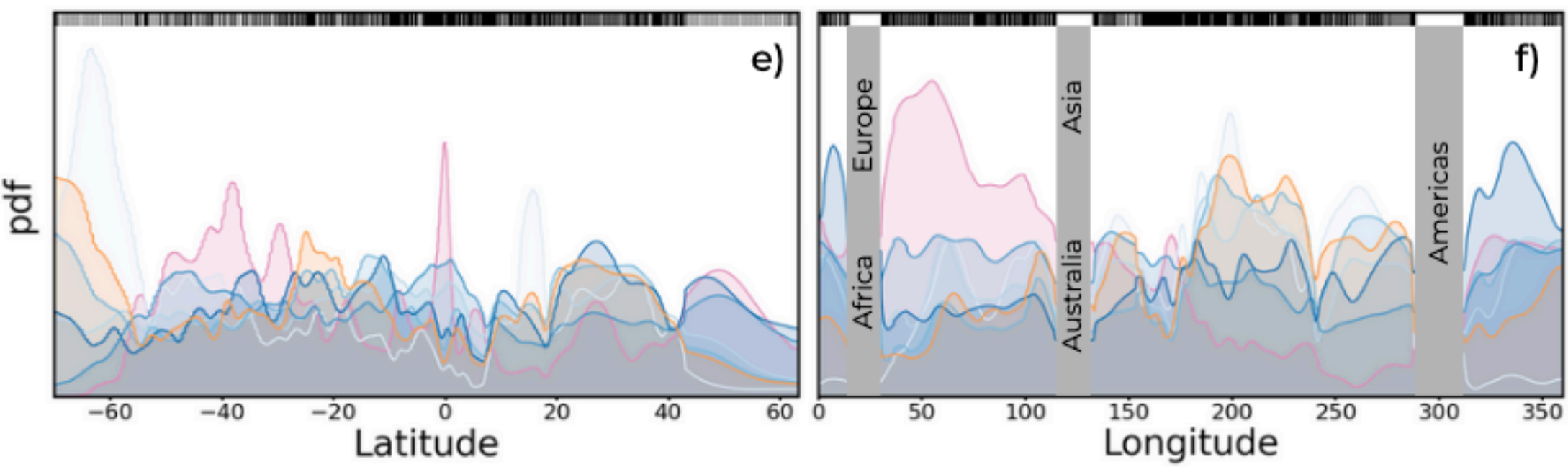
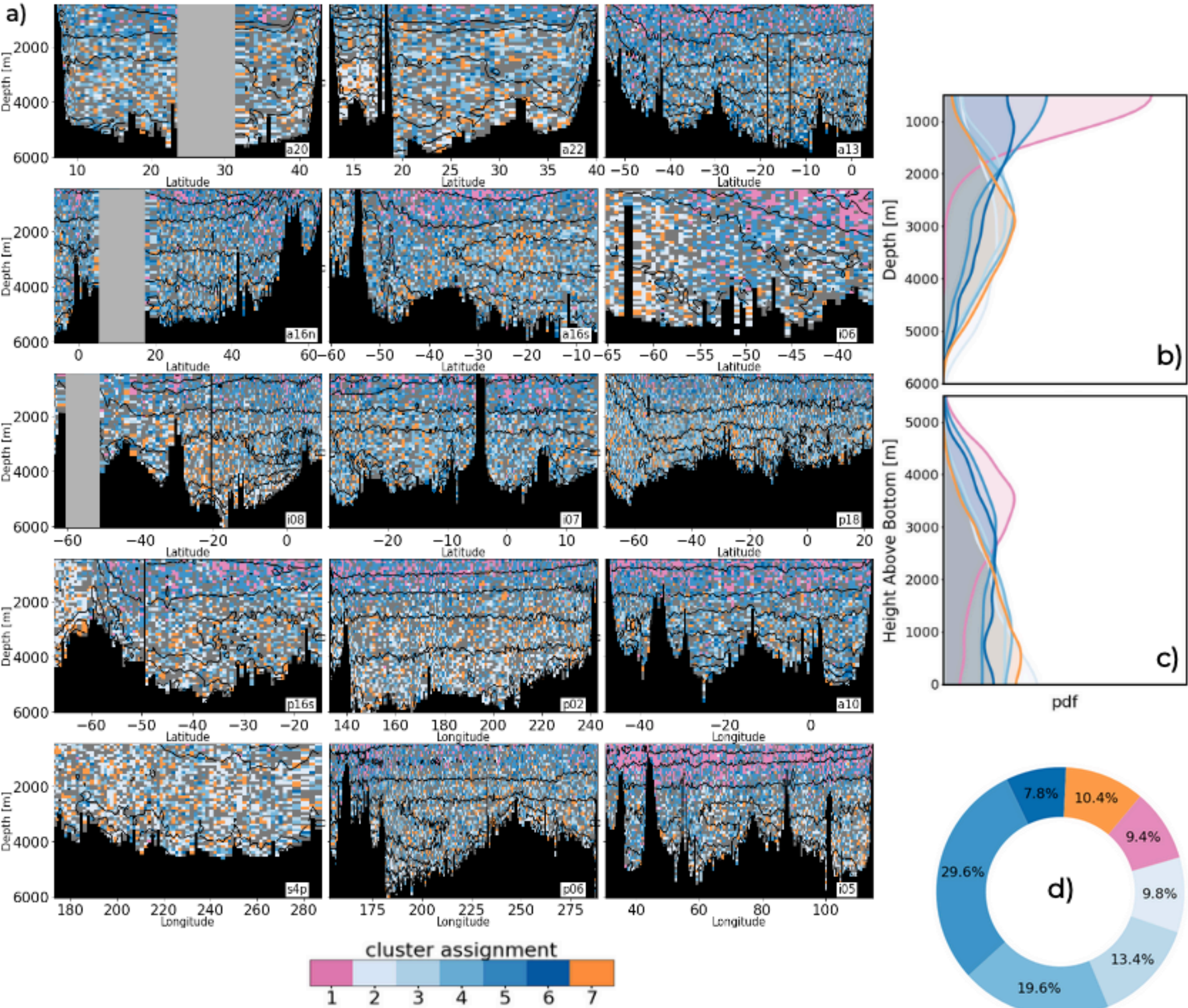


Figure 4.

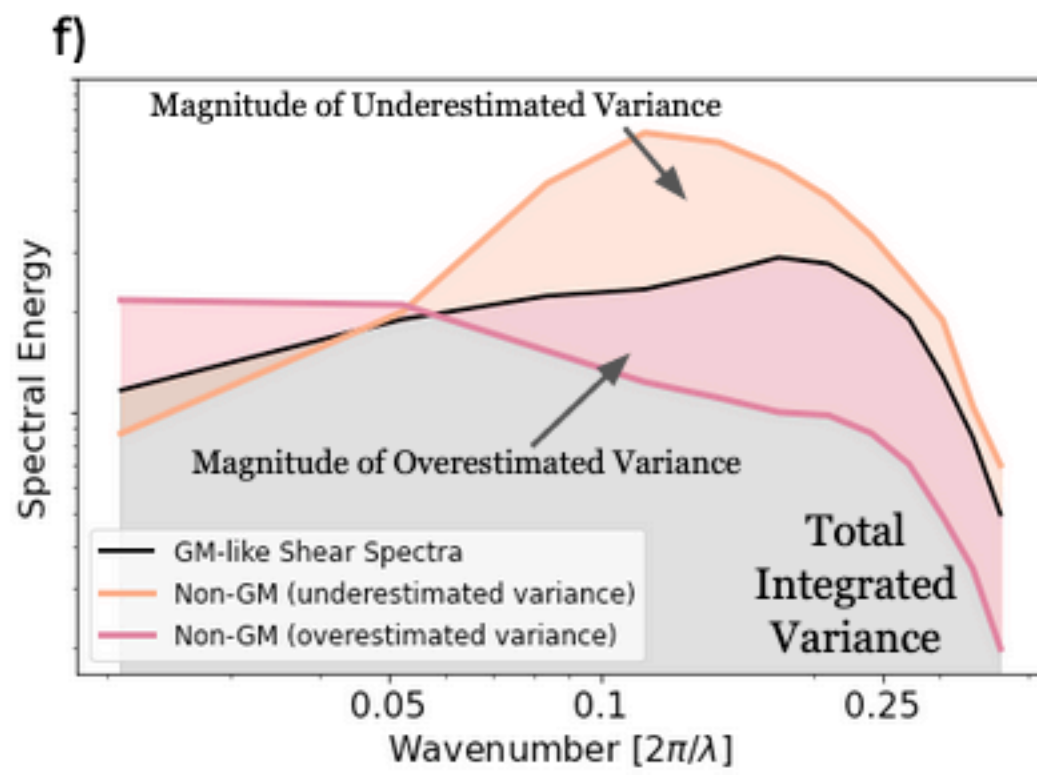
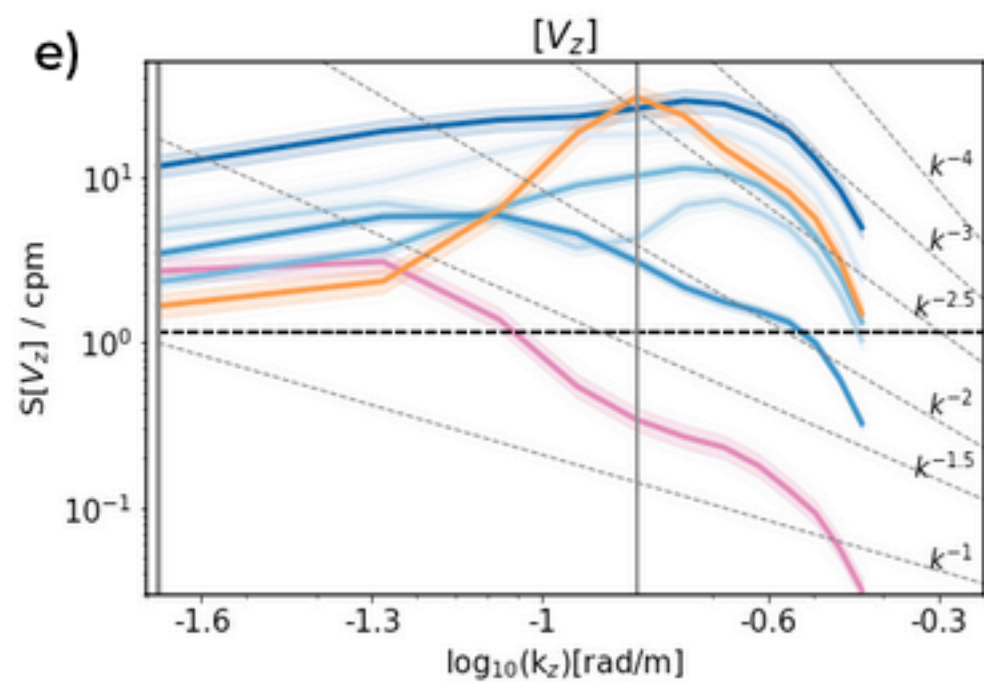
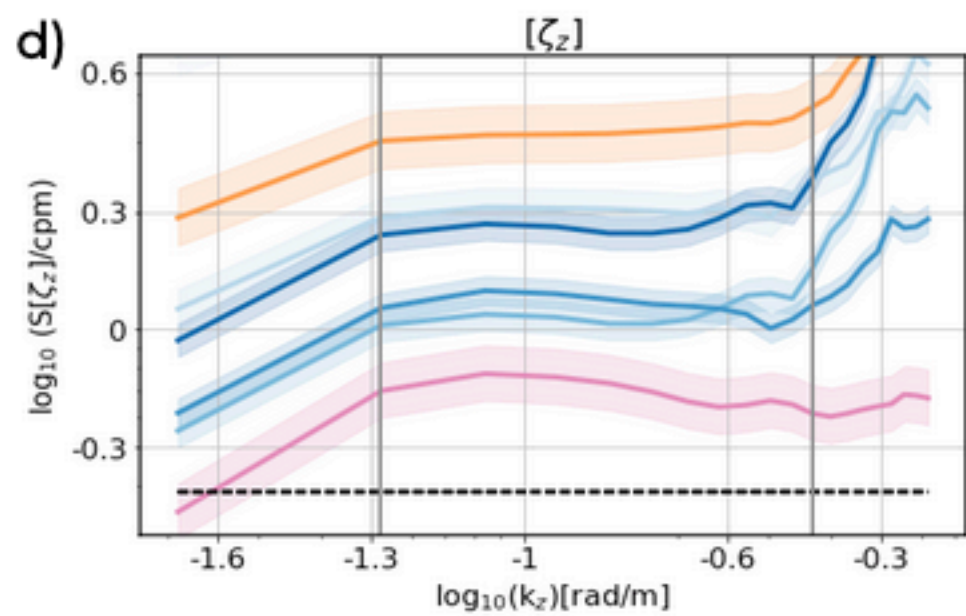
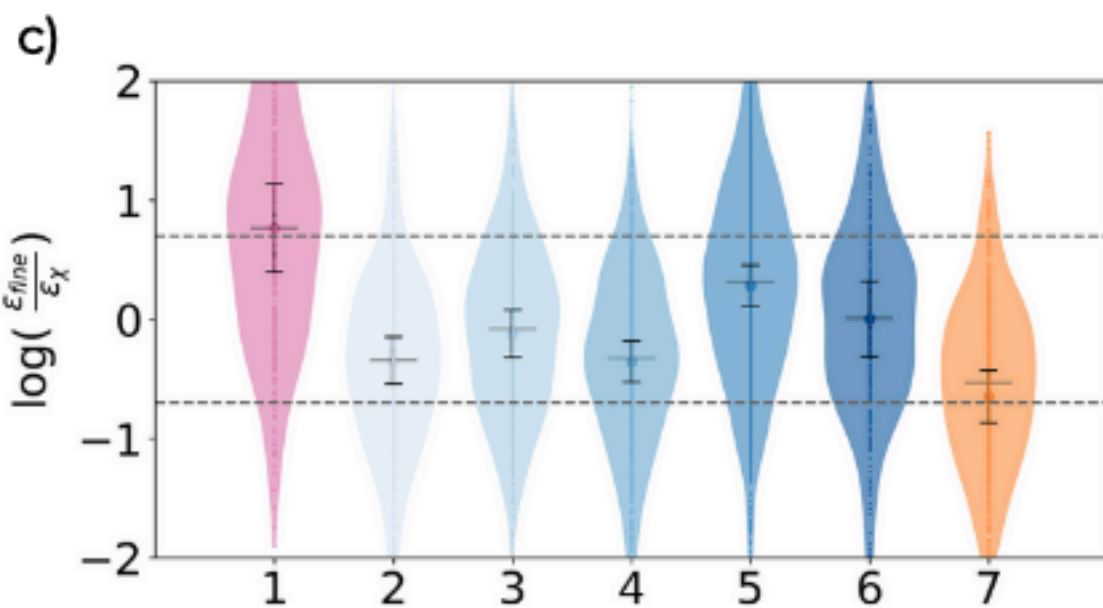
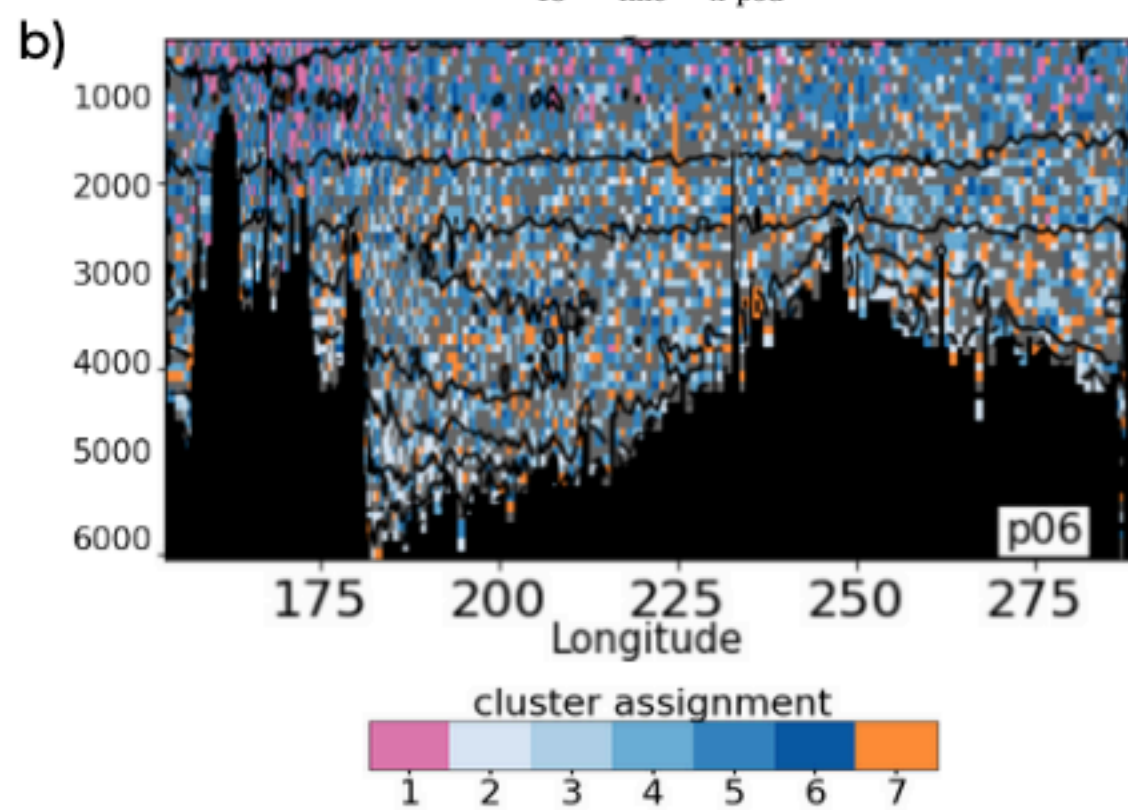
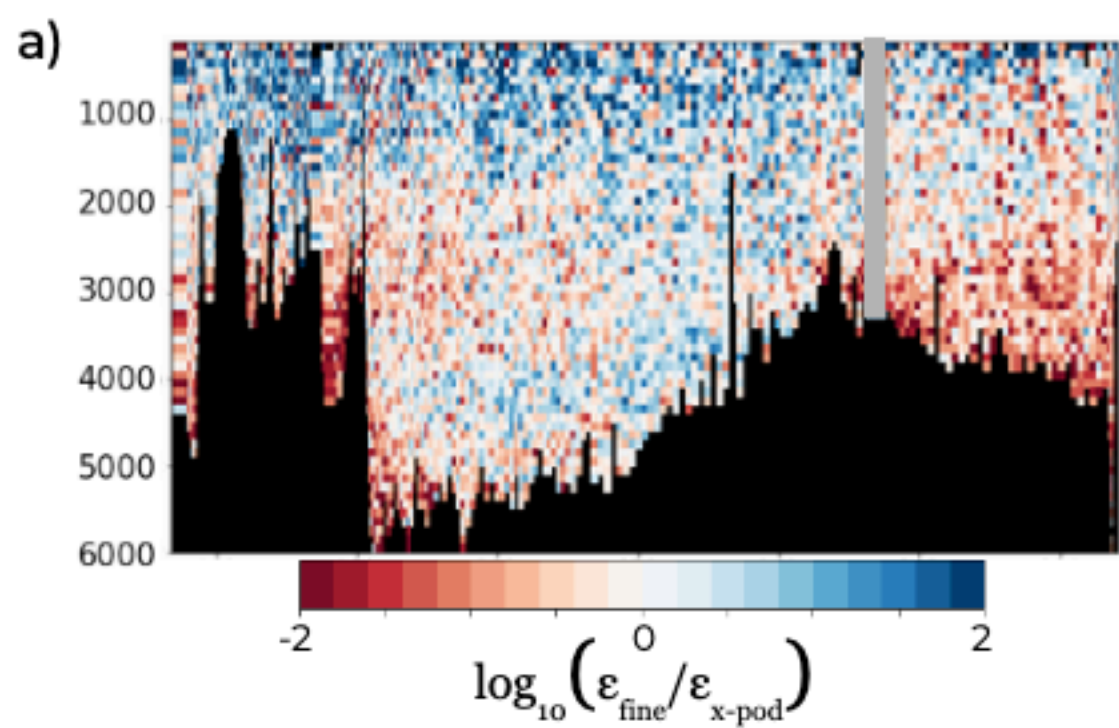
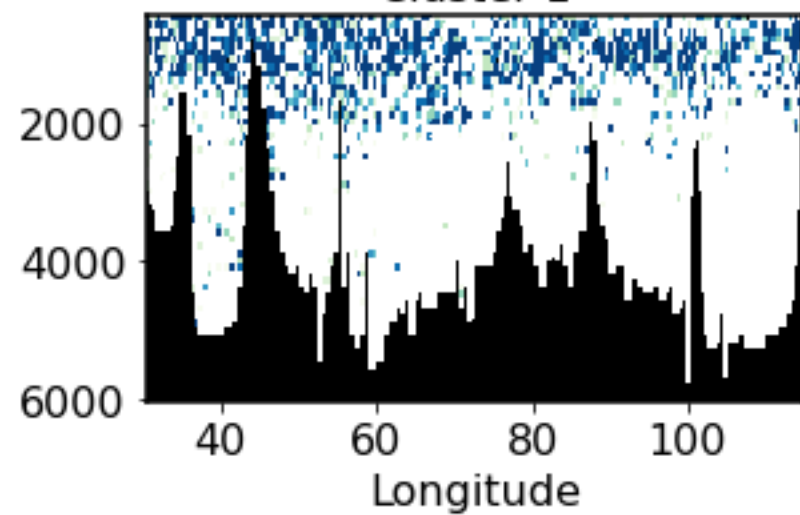
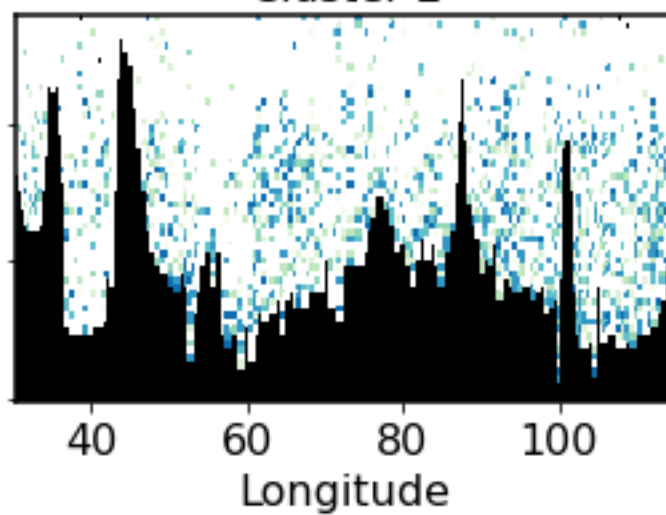


Figure 5.

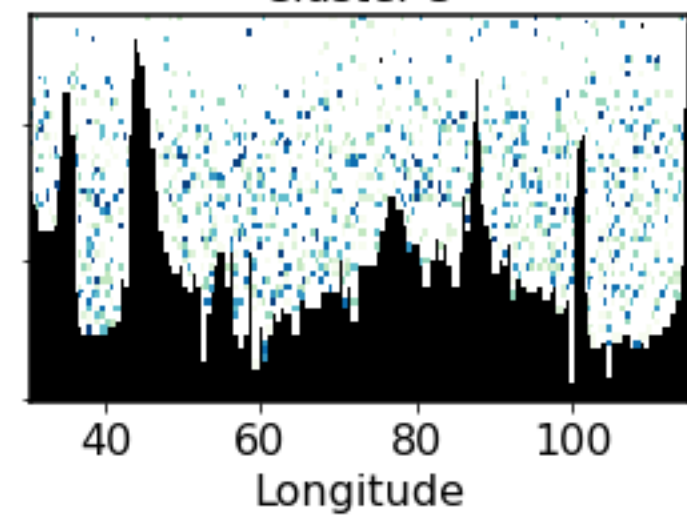
Cluster 1



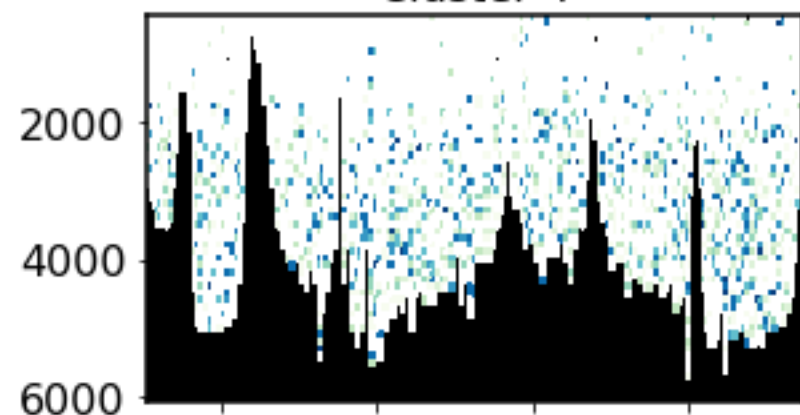
Cluster 2



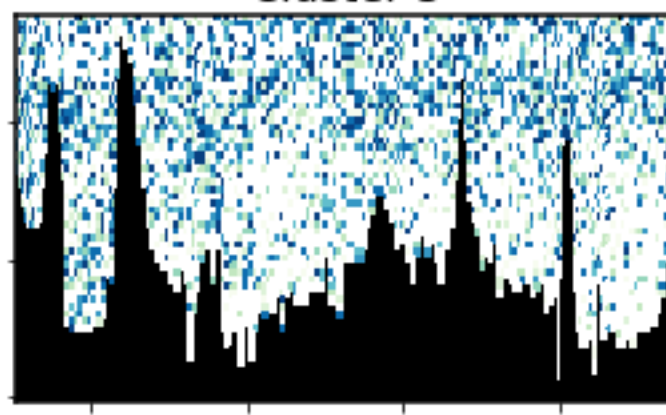
Cluster 3



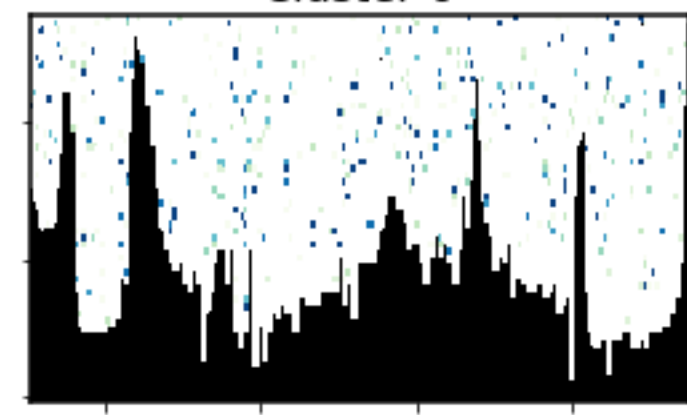
Cluster 4



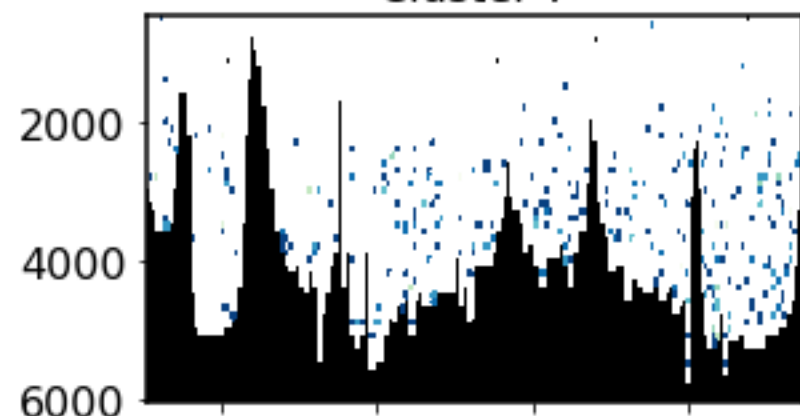
Cluster 5



Cluster 6



Cluster 7



posterior probability [%]

20 40 60 80 100

Figure 6.

I05

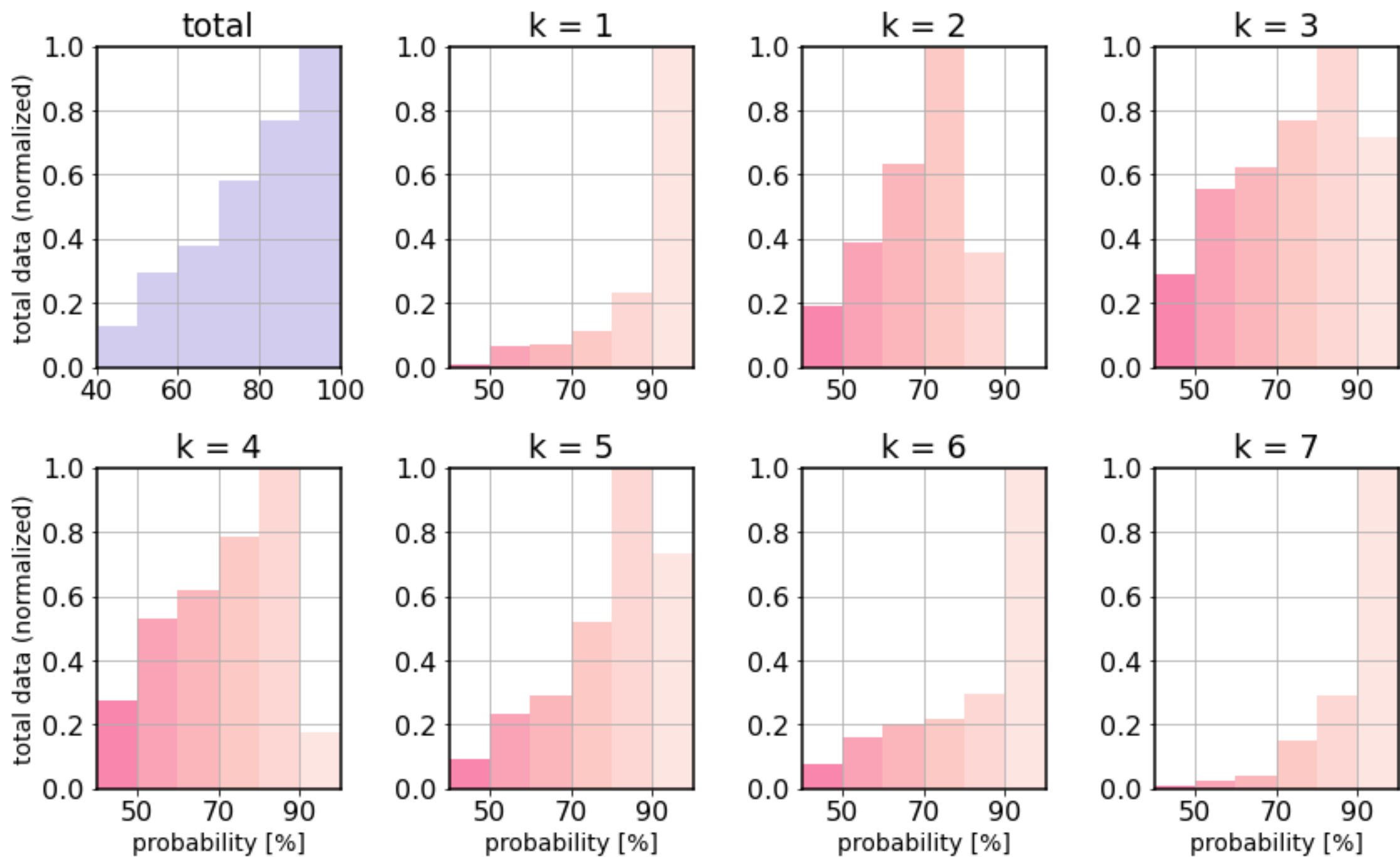


Figure 7.

1e6

